Microstructural and magnetic characterization of Ni0.5Zn0.5Fe2O4 ferrite nanoparticles

A. Bajorek, Clément Berger, M. Dulski, P. Łopadczak, M. Zubko, K. Prusik, M. Wojtyniak, A. Chrobak, Fabien Grasset, N. Randrianantoandro

Microstructural and magnetic characterization of $Ni_{0.5}Zn_{0.5}Fe_2O_4$ ferrite nanoparticles

A. Bajorek[1,2], C. Berger[3], M. Dulski[2,4], P. Łopadczak[1,2],M. Zubko[2,4], K. Prusik [2,4],M. Wojtyniak[1,2], A. Chrobak[1,2],F. Grasset[6],N. Randrianantoandro[5]

[1] A. Chełkowski Institute of Physics, University of Silesia in Katowice, 75 Pułku Piechoty 1, 41-500 Chorzów, Poland,
[2] Silesian Center for Education and Interdisciplinary Research, University of Silesia in Katowice, 75 Pułku Piechoty 1A, 41-500 Chorzów, Poland
[3] Université François-Rabelais, Greman, UMR 7347, 16 rue Pierre et Marie Curie, 31071 Tours, France
[4] Institute of Materials Science, University of Silesia in Katowice, 75 Pułku Piechoty 1A, 41-500Chorzów, Poland
[5]l'Institut des Molécules et Matériaux du Mans UMR CNRS 6283, Le Mans Université , Avenue Olivier Messiaen, 72085 Le MansCedex 9, France
[6]Laboratory for Innovative Key Materials and Structures (LINK UMI 3629), National Institute for Materials Science (NIMS), NIMS-Saint-Gobain Center of Excellence for Advanced Materials, 1-1 Namiki, Tsukuba, Ibaraki 305-0044, Japan

Corresponding author: **Anna Bajorek**
e-mail: anna.bajorek@us.edu.pl

Phone: +48 32 3497582, Fax: +48 32 258-84-31

Corresponding address: A. Chełkowski Institute of Physics, University of Silesia, Silesian Center for Education and Interdisciplinary Research, 75 Pułku Piechoty 1A, 41-500 Chorzów, Poland

Authors:
Clement Berger, e-mail: clement.berger@univ-tours.fr

Mateusz Dulski, e-mail: mateusz.dulski@us.edu.pl

Paweł Łopadczak, e-mail: pawel.lopadczak@smcebi.edu.pl

Maciej Zubko, e-mail: maciej.zubko@us.edu.pl

Krystian Prusik, e-mail: krystian.prusik@us.edu.pl

Marcin Wojtyniak, e-mail: marcin.wojtyniak@us.edu.pl

Artur Chrobak, e-mail: artur.chrobak@us.edu.pl

Fabien Grasset, e-mail: fabien.grasset@univ-rennes1.fr

Nirina Randrianantoandro, e-mail: Nirina.Randrianantoandro@univ-lemans.fr

Abstract

The comprehensive study of the $Ni_{0.5}Zn_{0.5}Fe_2O_4$ ferrite nanopowder crystallized in the inverse spinel structure and synthesized by co-precipitation method is presented. The distribution of Fe^{3+} cations among tetrahedral and octahedral sites was confirmed. The microstructural investigations revealed the presence of ultrafine grained structure with an average crystallites size in the range of $14 \div 20$ nm. Raman and Fourier-Transform Infrared (FTIR) spectroscopy studies confirmed typical spinel structure with tetrahedrally and octahedrally iron occupancy as well as indicate co-associated iron-oxide phases considered as factors responsible for the structural disorder. The magnetic properties revealed the superparamagnetic behavior at the room temperature with estimated critical size of single domain particles about 63 nm. The analysis of saturation magnetization pointed to the spin canting phenomenon in the surface layer. The valuation of exchange coupling parameters based on the mean field theory calculation strengthened the conclusion about opposite magnetization arrangement between tetrahedral and octahedral magnetic sublattices.

Keywords

Ni–Zn nano ferrites, Nanoparticles, Microstructure, Magnetic properties, Crystal and electronic structure

Highlights

- co-precipitated $Ni_{0.5}Zn_{0.5}Fe_2O_4$ nanoferrite addopt the cubic inverse spinel ferrite structure
- the average nanocrystallites/nanoparticles size estimated by TEM is about 15 nm
- Fe^{3+} cations are distributed at A – tetrahedral and B – octahedral sites
- studied nanoferrite reveals the superparamagnetic nature at the room temperature
- the canting spin effect was confirmed based on magnetic measurements

Graphical abstract

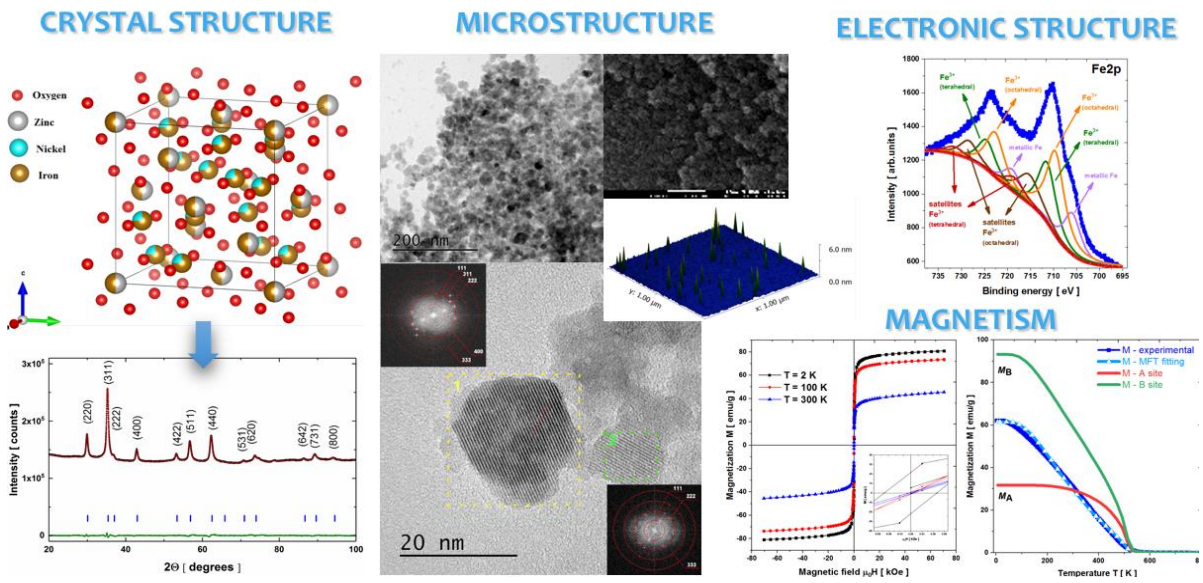

1. Introduction

Spinel ferrite nanoparticles (SF-NPs) adopting the general $A^{2+}Fe_2^{3+}O_4$ formula with A = Ni [1–17], Ni-Zn [1,2,8,18–59], Mn [1,60–62], Co [1,60,61,63–73], Co-Zn [74–79], Ni-Cu[43], Zn[80–85], Mn-Zn [17,86], Mg [61,87] are widely studied over years due to their potential applications in electronics e.g. as memory storage devices, permanent magnets, power transformers, telecommunications devices, magnetic fluids as well as photocatalytic and biomedical application e.g. as targeted drug delivery, hyperthermia or cancer treatment [1,2,16,18,41]. Generally, SF-NPs may indicate inverse spinel structure, where Fe^{3+} and A^{2+} cations are distributed over tetrahedral and octahedral sites or normal spinel structure where A^{2+} cations are placed at tetrahedral site whereas Fe^{3+} at octahedral sites [1,21,28,32,36]. The control of crystal structure and microstructure by applying various synthesis methods e.g. microwave [19,63], sol-gel [7,44,49,56,74,88], self - combustion [7,10,24,36,49,51,52,56,74], hydrothermal precipitation [4,20], mechanical alloying [28,35,53,54], solvothermal [5,60], co-precipitation [6,39,46,48,49,69,73,76] and others [14,15,22,23,25–27,29,34,43,67,77,89,90] allows to design and produce nano ferrites without drawbacks typical for their bulk counterparts [21]. The applied type of confinement leads to various properties typical at nanoscale like superparamagnetism, core-shell structure or spin - glass systems [18]. Taking into account the potential applications a thorough analysis of the effect of dopants on nano ferrites properties is usually conducted. Furthermore, it is desired to develop low – cost synthesis methods, which will lead to enhancement of applicable SF – NPs parameters.

Among a large number of various investigated spinel nano ferrites a lot of attention has been recently focused on nickel – zinc-based materials [1,2,18–32,34–54,56–59,89].Generally, the mixed Ni – Zn type of ferrites revealed quite a high resistivity, high permeability, high values of the saturation magnetization and Curie temperature, high mechanical hardness [2]. They also demonstrate a very good chemical stability and dielectric properties [20]. Moreover,

doping of $NiFe_2O_4$ by non - magnetic Zn results in the modification of the AB_2O_4 – type of crystal structure by cations redistribution in the crystal lattice as well as in the change of the microstructure, magnetic and electric properties, spin glass behavior, core-shell type of magnetism and non – collinear spin structure [1,18]. The above-mentioned properties can be controlled and are strictly dependent on the amount of Zn content and the type of synthesis procedure [1,2,18,21–32,34–54,56–59,89,89]. Thus, structural and magnetic properties are interrelated and dependent occasions distribution and synthesis route. Generally, increasing the zinc amount is reflected in the increase of lattice parameter due to the large ionic radius of Zn^{2+} compared to Ni^{2+} [38,43]. As a consequence, the crystallites/grains size is slightly modified of about 10 nm depending on synthesis procedure [20,24,38,43]. As it was previously evidenced by *Vasoya et al.* [28] applying the ball – milling method into $Ni_{0.5}Zn_{0.5}Fe_2O_4$ induces temperature diffuse scattering forcing the preferred orientation of grains. The occupation of Zn^{2+} cations in B – site was estimated based on XRD as 50 - 60% due to a slight modification in synthesis procedure. Furthermore, lattice parameter and strain, surface area and energy were strictly dependent on milling duration. The saturation magnetization (M_S) in bulk $Ni_xZn_{1-x}Fe_2O_4$ ferrites was estimated as the highest for x = 0.5 [24]. However, for nanoscale materials the maximum may be moved due to particles size and surface effect caused by generating the non – collinear structure in the surface layer. Nonetheless, the collinear structure can be maintain in the entire volume of the particle as it was shown by *Kavas et al*. [20], who applied the PEG assisted hydrothermal method in the synthesis process. On the other hand *Zhang et al.* [24] showed that in the case of sol-gel auto combustion type of synthesis the maximum of M_S is noticed for x = 0.7, which is caused by the non-collinear spin configuration on the surface. Similar behaviour was observed by *Slatineanu et al* [32], who used the same kind of production method and pointed to the maximum M_S for x = 0.2. The chitosan synthesis route invented by *Gabal et al.* [43] pointed to the maximum M_S value for x = 0.4 followed by its decrease with

further doping. The amount of zinc content was also had an impact on the coercivity (H_C), which due to magnetocrystalline anisotropy was enhanced with lowering of x [24,43]. Among all used synthesis methods of Ni – Zn nano ferrites one may indicate co-precipitation, which is distinguished by its relatively ease in preparation, quite good homogeneity and a relatively narrow range in particles size distribution. Such method was applied by *Srinivas et al.* [46], who evidenced that Ni doping lead to lattice shrinkage with simultaneous increase of grain size. Additionally, he pointed to the core-shell like magnetic behavior and superparamagnetism at the room temperature for $x = 0.5 – 0.7$. On the other hand *Kumar et al*. [30] revealed the small hysteretic behavior at 300 K for $x = 0.5$ and claimed that it can be a prove of ferromagnetic arrangement. He also noticed, that higher Zn concentration is reflected in superparamagnetic behavior. The AC conductivity for the co-precipitated Ni - Zn specimens produced and studied *Kasam et al.* [48] was found as sensitive for concentration of Ni ions. It was shown, that the increase of Ni^{2+} is reflected in reduction of conductivity due to the domination of electronic conductivity over ionic conductivity.

The diversity of the observed phenomena dependent on the choice of synthesis process makes these materials extremely attractive for basic research and at the same time the optimization of their potential remarkable application properties is a challenge for functionalization of Ni – Zn based ferrites. Bearing in mind the fact, that the analysis of ferrite properties in recent years has been of particular concern to many research groups, we wanted to expand the existing state of knowledge. Therefore, herein we were focused on the microstructure and magnetic properties of $Ni_{0.5}Zn_{0.5}Fe_2O_4$ nanopowder fabricated by co-precipitation method. The various complementary measurements techniques were applied by us in order to accurately describe and understand the mutual relation between structure and magnetism in synthesized nano ferrites. Nevertheless, we want to underline that for such system no one has so far performed a comprehensive analysis of magnetic properties with an indication

of the spin-canting phenomenon of iron magnetic moments and the participation of only trivalent iron ions distributed in the tetrahedral and octahedral state.

2. Materials and methods

2.1. Synthesis

The $Ni_{0.5}Zn_{0.5}Fe_2O_4$ nanoparticles were synthesized by the co-precipitation route from elements having a purity higher than 99% (nickel chloride $NiCl_2$, $6H_2O$ from Wako laboratory; iron chloride – $FeCl_3$, $6H_2O$, heptane, surfactants and TEOS from Aldrich laboratory; zinc acetate $ZnAc_2$, $2H_2O$ from Fluka laboratory and ammonia 25% from Merck laboratory.

Metallic salts (nickel and iron chloride and zinc acetate) were weighed in a molar ratio of 1 according to stoichiometric formula. A solution of 0.04 mol iron chloride (18.8116g - $FeCl_3$, $6H_2O$), 0.01 mol of nickel chloride (2.376g - $NiCl_2$, $6H_2O$) and 0.01 mol of zinc acetate (2.376g - $ZnAc_2$, $2H_2O$) are poured as quickly as possible under vigorous stirring to the alkaline solution of NaOH (250 ml per 1 mol/l), which is subsequently heated at 95°C for 90 minutes and cool down to the ambient temperature.

The obtained precipitate was separated from the liquid by two-step centrifugation process: (1) separation - 4000 rpm for 10 minutes, (2) washing in a distilled water and separation - 400 rpm for 10 minutes. After such treatment agglomerates of nanoparticles were obtained. Subsequently, they were dispersed into the solution of nitrate HNO_3 (25 ml to 1mol/l) for 15 min under vigorous stirring. Such treatment was applied in order to create surface charge as a way to promote electrostatic repulsion essential for ferrofluids synthesis. After adding an acetone the precipitate was once again centrifuged 4000 rpm for 15 minutes. The double rinsing in acetone was required to eliminate NO^{3-} [a] charge which screens the positive charge on the surface of nanoparticles and afterward a separation by centrifugation process 1650 rpm for 10 min was applied. The obtained powder was dried in the air for 48 hours.

2.2. Characterization

The crystal structure was examined by means of X-ray Powder Diffraction (XRD) using Empyrean PANalytical diffractometer equipped with Cu X-ray source ($K_{\alpha 1}$ of 1.54056 Å) with the Bragg-Brentano geometry θ-2θ. The obtained results were processed in the MAUD software [91].

The particles size was determined by Dynamic Light Scattering (DLS) Zetasizer Nano ZS Malvern Instruments. The measured sample was suspended in about 10 ml of ethanol in a glass cell. The measurement was performed after setting Zetasizer instrument into 173° configuration and applying the appropriate standard operating procedure (SOP) based on statistical measurements.

Raman experiment was performed using WITec confocal Raman microscope CRM alpha 300 equipped with an air-cooled solid-state laser (λ = 532 nm) and a CCD camera. The excitation laser radiation was coupled into a microscope through a single-mode optical fiber with a 50 mm diameter. An air Olympus MPLAN (100x/0.90NA) objective was used. Raman scattered light was focused on a multi-mode fiber (50 mm diameter) and monochromator with a 600 line/mm grating. Raman data were accumulated through low laser power (1 mW) due to problems described by *Ahlawat and Sathe* [92]. The spectra were collected by 30 scans with an integration time of 20 s and resolution of 3 cm^{-1}. The spectrometer monochromator was calibrated using the Raman scattering line of a silicon plate (520.7 cm^{-1}).

Fourier-Transform Infrared spectroscopy (FTIR) measurements were performed using an Agilent Cary 640 FTIR spectrometer equipped with a standard source and a DTGS Peltier-cooled detector. The spectra were collected using GladiATR diamond accessory (Pike Technologies) in the 4000 - 400 cm^{-1} range with a spectral resolution of 4 cm^{-1} and recorded by accumulating of 16 scans. The water vapor and carbon dioxide were subtracted from the

spectrum. Finally, the baseline correction and peak fitting analysis of all spectra by Voigt function was performed using GRAMS software package.

The Scanning Electron Microscopy (SEM) was performed with a JEOL JSM-7100F FEG (field emission gun) high-resolution scanning electron microscope (HR-SEM) operated at 15 kV in SE (Secondary Electron) mode.

The Transmission Electron Microscopy (TEM) studies were performed with the use of Jeol JEM 3010. First, the measured sample suspended in ethanol was placed in the ultrasonic washer for 2 h in order to fracture agglomerates. Next, a few drops such mixture were placed on the carbon coated Cu grid (400 mesh). As usual, TEM and HRTEM images were recorded for more than one region of interests.

The Atomic Force Microscopy (AFM) measurements were performed at room temperature using tapping mode and standard silicon tip. The liquid solution of the studied specimen dispersed in ethanol was placed onto freshly cleaved mica substrate and dried up prior to the ambient temperature.

All X-ray Photoemission Spectroscopy (XPS) results were obtained at room temperature by using monochromatized X-ray source Al K_α (1486.6 eV). The sample was fixed into the sample holder by double coated conductive carbon tape and subsequently was stored under ultra-high vacuum for a weak. Next, the XPS measurement was performed in four consecutive steps. In the first one, the as-prepared material was studied directly after its storage. Afterwards, the same specimen was sputtered by Ar^+ ion beam for 15 min (2 step), 30 min (3 step) and 45 min (4 step) and after each ion cleaning the sample was measured. All the obtained XPS spectra were calibrated using C1*s* peak (BE = 284.8 eV) as carbon peak usually originates from the carbon adsorbed on the surface of the sample and used as a reference for charge correction. All measured spectra were processed with the use of MultiPak 9.2 software.

The magnetic properties were determined based on wide-range Superconducting Quantum Interference Device (SQUID) magnetometer MPMS XL7 Quantum Design, temperature from 2 K to 400 K and magnetic field up to $\mu_0 H = 7$ T. The AC measurements were acquired at different frequencies: 1 Hz, 10 Hz, and 100 Hz. The DC measurements were collected in field cooled (FC) and zero field cooled (ZFC) modes at the external field of 100 Oe and 1000 Oe. The hysteresis loops were recorded at 2 K, 100 K, and 300 K.

Mössbauer spectra collected at a temperature higher than 77 K were recorded with the use of a standard transmission geometry equipped with a conventional constant acceleration spectrometer and a ^{57}Fe source diffused into a Rh matrix. All spectra recorded at 4.2 K and under external field used a cryomagnetic device equipped with a superconducting coil which can provide a magnetic field ranging from 0 to 8T. Every run of measurement took about about 24h at high temperature and less for low temperature (< 77K) due to increases of f-factor which favorites the measurement. A spectrum calibration was made with pure α-Fe powder.

3. Results and discussion

3.1. DLS results

In order to evaluate an average size of as-obtained particles, its evolution, and distribution over milling process the dynamic light scattering (DLS) method was applied. It is well known that DLS technique is based on the Brownian motion of the particles or molecules suspended in a liquid solution, which causes the scattering of the laser light at different intensities. The analysisof the intensity fluctuations over time yields the velocity of the Brownian motion. Hence, smaller particles move faster than bigger ones and the particle size is calculated using the following Stokes-Einstein equation:

$$D_H = \frac{k_B T}{f} = \frac{k_B T}{3\pi\eta D} \qquad (1)$$

where: D_H - hydrodynamic diameter of the particles,f - particles friction coefficient, k_B - Boltzmann constant, η - viscosity of the solvent, D - diffusion coefficient.

Thus, the DLS method provides information on the distribution of the particle diameters. For the mono-disperse system comprising spherical particles the particle size distribution histogram (PSD) consists of one narrow peak. The heterogeneous (poly-dispersed) mixtures with particles having different sizes and shapes are characterized by ahigher index of poly-dispersity (PDI). Thus, the PSD histogram is usually wide, with more than one peak. During DLS experiment the intensity autocorrelation function of the light scattered by particles is measured. Subsequently, such function is fitted in order to obtain the particles size via two different fitting algorithms. The first one (*cumulant method*) results in an overall average size (Z – average) and PDI index values. The second method (*distribution method*) gives a distribution of particle sizes with an average (mean) size and width for each separate size peak in the PSD histogram. For a perfect monodispersed samples, mostly with spherical particles, these two approaches should give the same results with one peak in PSD histogram and relatively low PDI.

Here we have analyzed three types of particles size distributions (see Figure 1): intensity, volume, and number. In the first one, the particle size is related to the amount of light refracted by the particles and the latter two are converted from the based intensity distribution based on *Mie* theory [91,92] describing the relative proportion of multiple components in the sample based on their volume/number rather than based on their scattering.

In our case, the value of obtained mean particles sizes from three type of histograms is about: 1169 nm ± 492 nm (intensity), 1121 nm ± 380 nm (volume) and 949 nm ± 259 nm (number). Similarly, the value of Z - average is about 1113 nm ± 78 nm and PDI index equal 0.171 ± 0.011 suggesting rather homogeneous and monodisperse nature of the studied specimen. Nonetheless, the estimated particles size is rather large, which may suggest partial

agglomeration of studied nanoparticles due to van der Waals forces and magnetic dipolar interactions.

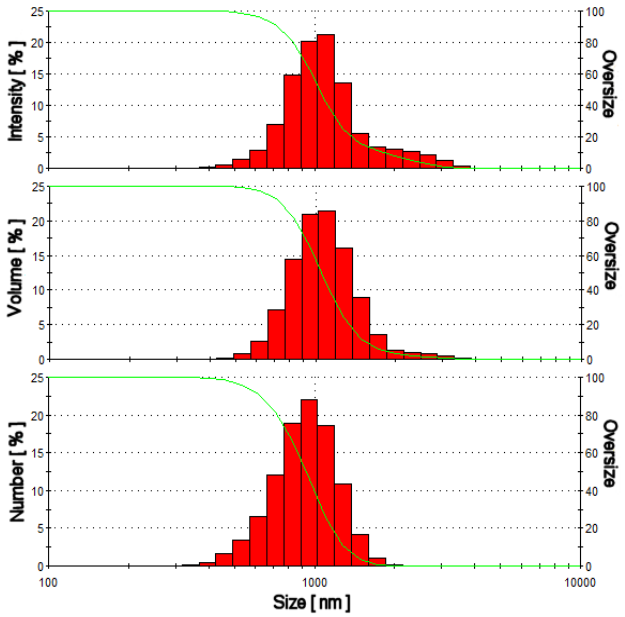

Figure 1. The intensity (a), volume (b) and number (c) particle size distribution (PSD) histograms for the $Ni_{0.5}Zn_{0.5}Fe_2O_4$ sample.

3.2. X-ray diffraction

The studied ferrite nanopowder crystallizes in the spinel structure, which adopts a cubic symmetry with the *Fd-3m* space group. In such a structure, A^{2+} and B^{3+} cations occupy the octahedral sites (16d) or the tetrahedral sites (8a) depending on their lattice environments. Generally, we can distinguish two types of spinel ferrites due to various A^{2+} and Fe^{3+} cations distribution on A or Fe sites: the direct type of spinel noted as AB_2O_4 with the formula assigned as $[A^{2+}]^A[Fe^{3+}Fe^{3+}]^BO^{2-}$ and the inverse spinel noted as $B(AB)O_4$adopting the formula $[A^{2+}Fe^{3+}]^A[A^{2+}Fe^{3+}]^BO^{2-}$ [21,28,32]. Generally, in bulk Ni – Zn ferrites Ni^{2+} cations occupy *B-sites whereas* Zn^{2+} cation is placed at *A-sites. However, at the nanoscale, they are distributed randomly between A and B sites.*

The studied $Ni_{0.5}Zn_{0.5}Fe_2O_4$ nanopowder crystallizes in the inverse spinel structure. So, Ni^{2+} is preferentially located at B - octahedral site, whereas Fe^{3+} is uniformly distributed at A-

tetrahedral and B - octahedral sites. The Zn^{2+}, which is rather non-magnetic, nominally substituted in place of 50% of Ni^{2+} is preferentially distributed over A- tetrahedral site forcing some of the theFe^{3+} ions for transferring to B - octahedral site. Figure 2a represents the inverse spinel ferrite unite cell generated based on the crystal structure refinement, which was carried out with the use of MAUD software. The refinement result is illustrated in Figure 2b exhibiting experimental, calculated and difference signals. The presence of only one expected spinel cubic crystal phase was revealed. The low values of various factors (R_b, R_{wp}, R_{ex}) confirm a satisfactory quality of applied refinement procedure. All refinement parameters are placed in Table 1.

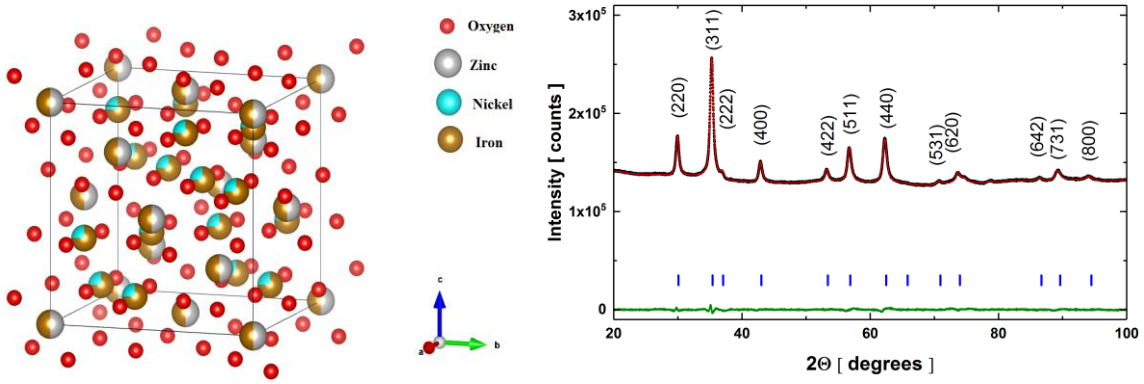

Figure 2. (a) The unit cell generated based on structure refinement and (b) XRD pattern for the $Ni_{0.5}Zn_{0.5}Fe_2O_4$ ferrite powder.

The estimated value of the lattice parameter a_{exp} equals 8.4286(7)Å and is in a good agreement with previously obtained [24,30,36,46,48]. The small discrepancy between the reported value and the experimental one may arise from some difference in cations distribution, which in nanoferrites are sometimes randomly redistributed over A and B sites [46]. The size of crystallites and lattice strain was estimated based on the crystal structure refinement. As it was evidenced in other Ni-Zn ferrites, the lattice strain is dependent on zinc content in the ferrite formula [37]. Doping of Ni^{2+} ions in the Zn^{2+} site leads to the reduction of lattice strain due to a smaller value of Ni^{2+} ionic radius, which also causes the increase in the crystallites size. In our case, the obtained value of d_{cryst} confirms the presence of ultrafine structures in the

examined specimen with an average crystallite size of 20.38 ± 0.02 nm and the estimated value of the lattice strain equals $\varepsilon_{RMS} = 1.442 \times 10^{-3}$, which is typical for nanostructured ferrites.

Table 1. Crystal structure parameters for the $Zn_{0.5}Ni_{0.5}Fe_2O_4$ nanopowder spinel ferrite.

Atom	**x**	**y**	**z**	**Occ.**	**B_{iso}**
Zn (A site)	0	0	0	0.5	0.26737 ± 0.02644
Fe (A site)	0	0	0	0.5	0.26737 ± 0.02644
Fe (B site)	0.625	0.625	0.625	0.75	0.17159 ± 0.02266
Ni (B site)	0.625	0.625	0.625	0.25	0.17159 ± 0.02266
O	0.3815	0.38157	0.38157	1.0	0.20540 ± 0.03934
Lattice parameter a_{exp}[Å]	$8.42867 \pm 6.16478 \times 10^{-5}$				
Unit-cellvolume V [Å^3]	593.233390				
Crystallites size d_{cryst}[nm]	20.38 ± 0.02				
Lattice strain ε_{RMS}	$1.442 \times 10^{-3} \pm 2.944 \times 10^{-5}$				
Interatomic distances [Å] A – A B - B A – B A – O B – O O - O	5.94146 2.97073 3.48349 1.92835 2.03955 2.79249				
Refinement factors [%] R_b R_{exp} R_{wp}	0.3016823 0.27144992 0.4115931				
δ [line/m^2] × 10^{14}	1.26	**P [%]**	72.6	**S[m^2/g]**	55.3
$\rho_{X\text{-}ray}$ [g/cm^3]	5.32		ρ_{bulk} [g/cm^3]		1.46
r_A [Å]	0.69		**r_B [Å]**		0.48
u_{exp} [Å]	0.3933		**u_{theor} [Å]**		0.3521
d_{AL} [Å]	2.0895		**d_{BL} [Å]**		1.9726
d_{AE} [Å]	3.4061	**d_{BES} [Å]**	2.5361	**d_{BEU} [Å]**	2.9967
L_A [Å]	3.6454		**L_B [Å]**		2.9711

Based on XRD results one may estimate the dislocation density, which is a measure of the number/length of dislocation per volume of the unit cell and represents the number of defects in a crystal. The dislocation density δ for spinel ferrites may be estimated as [44,45]:

$$\delta = \frac{15\,\varepsilon_{RMS}}{a\,d_{cryst}} \qquad (2)$$

where ε_{RMS} represents the lattice strain, a is the lattice parameter and *crystal* is the average crystallite size. Thus, the obtained value is about 1.26×10^{14} line/m^2, which is quite low comparing to other ferrites [61,87] confirming good crystallinity of the co-precipitated sample. The theoretical X− ray density ($\rho_{X\text{-}ray}$) was calculated using the following relation [46,61,87]:

$$\rho_{X-ray} = \frac{Z\,M}{N_A V} \qquad (3)$$

where Z = 8 and denotes the number of molecules per unit cell, M is the molecular weight, N_A is the Avogadro's number $N_A = 6.023 \times 10^{23}$ and V is the volume of the unit cell. The calculated value equals $\rho_{X\text{-}ray}$ = 5.32g/cm^3, which is close to that obtained for other nanoferrites [46]. The specific surface area (S) estimated by the following relation:

$$S = \frac{6}{\rho_{X-ray}\,d_{cryst}} \qquad (4)$$

equals about 55.3m^2/g and is quite large comparing to other ferrites [28,61,87] due to ahigh degree of crystallinity and relatively low value of $d_{cryst,}$ confirming the large value of surface to volume ratio. Based on the value of $\rho_{X\text{-}ray}$ and the value of bulk density ρ_{bulk} expressed as:

$$\rho_{bulk} = \frac{m_{sample}}{V_{sample}} \qquad (5)$$

the porosity (P) of the investigated SF-NPs may be calculated from the equation:

$$P = \frac{100\left(\rho_{x-ray} - \rho_{bulk}\right)}{\rho_{x-ray}} \qquad (6)$$

The value of ρ_{bulk} = 1.46 g/cm^3 is relatively low comparing to previously reported for the same quantity of Zn [46,48], which is probably an effect of the difference in synthesis approach, in crystallites size and in the way of ρ_{bulk} estimation. The percentage porosity is quite large compared to others Ni – Zn ferrites [38,46], which may be related to the synthesis and ρ_{bulk} estimation routes.

Thus, the formula of the inverse ferrite spinel structure for the studied specimen may be described by the following formula $[Zn_{(1-x-a)}^{2+}Ni_{(x-b)}^{2+}Fe_{(a+b)}^{3+}]^A[Zn_{(a)}^{2+}Ni_{(b)}^{2+}Fe_{(2-(a+b)}^{3+}]^BO_4^{2-}$ [32], where x = 0.5 and based on Rietveld refinement other two parameters equal a = 0 and b = 0.5. Thus, the occupation within A - tetrahedral and B - octahedral sites and may be assigned as A = $Zn_{0.5}Fe_{0.5}$ and B = $Ni_{0.25}Fe_{0.75}$. It is worth noticing, that the isotropic displacement factors (B_{iso}) of the Zn^{2+} and Fe^{3+} cations distribution in the tetrahedral sites are larger than those in the octahedral sites. It may be caused by longer bond lengths.

According to the cations distribution of the theoretical ionic radius of a tetrahedral site (r_A) site and an octahedral site (r_B) may be calculated from the relations [61,87]:

$$\begin{aligned} r_A &= C_{AZn}\, r(Zn^{2+}) + C_{AFe}\, r(Fe^{3+}) \\ r_B &= \frac{1}{2}\left[C_{BNi}\, r(Ni^{2+}) + C_{AFe}\, r(Fe^{3+})\right] \end{aligned} \qquad (7)$$

where ca_n, C_{AFe}, C_{BNi}, C_{BFe} represents the concentration of Zn^{2+}, Fe^{3+} at A site and Ni^{2+}, Fe^{3+} at B site respectively whereas r denotes ionic radii for appropriate ions Zn^{2+} (r = 0.74Å), Fe^{3+} (r = 0.64Å), Ni^{2+} (r = 0.78Å). The values of A and Bite ionic radius was calculated as r_A = 0.69 Å and = 0.34 Å. Furthermore, the experimental (u_{exp}) and theoretical (u_{theor}) values of oxygen ion positional parameter may be calculated by the following equation [55,61,77,87]:

$$u = \left[(r_A + r_O)\frac{1}{a\sqrt{3}} + \frac{1}{4} \right] \qquad (8)$$

taking into account the experimental value of the *hex* lattice parameter obtained from Rietveld refinement and the theoretical value of the a_{theor} lattice parameter based on the equation [55,93]:

$$a_{theor} = \frac{8}{3\sqrt{3}}\left[(r_A + r_O) + \sqrt{3}(r_B + r_O)\right] \quad (9)$$

where r_O denote the O^{2-} ionic radius (r_O =1.4 Å). Usually, the parameter u depends on the chemical composition and samples preparation conditions and its value for spinel ferrites was reported as u = 0.375Å [55,61,87]. The deviation from such value may suggest some deviation from theoretical spinel structure probably caused by the synthesis conditions. Thus, it may arise from a small anions displacement due to the expansion of tetrahedral inter-sites [20]. The calculated value of u_{exp} equals 0.3933 Å and is slightly different from the theoretical one (u_{theor} = 0.3521 Å), which is caused by the difference between a_{exp} and a_{theor} probably related to the lattice defects for polycrystalline sample and the distribution of Fe^{3+} over A and B sites but may also arise for the synthesis procedure.

The tetrahedral bond length (d_{AL}) for d_{A-O}^{2-}, octahedral bond length (d_{BL})for d_{B-O}^{2-} as well as the tetrahedral edge length (d_{AE}), shared octahedral (d_{BES}) and unshared octahedral (d_{BEU}) edge lengths were calculated with the following formula [87]:

$$\begin{aligned} d_{AL} &= a\sqrt{3}\left(u - 1/4\right) \\ d_{BL} &= a\left[3u^2 - (11/4)u + 43/64\right]^{1/2} \\ d_{AE} &= a\sqrt{2}\left(2u - 1/2\right) \\ d_{BES} &= a\sqrt{2}\left(1 - 2u\right) \\ d_{BEU} &= a\left[4u^2 - 3u + 11/16\right]^{1/2} \end{aligned} \quad (10)$$

The hopping lengths which describe the distance between the magnetic ions in A and B sites, in our case probably between Fe^{3+} in A - site, and Ni^{2+}/Fe^{3+} in B -site can be calculated by the relations [55,61,77,87]:

$$\begin{aligned} L_A &= a\sqrt{3}/4 \\ L_B &= a\sqrt{2}/4 \end{aligned} \quad (11)$$

All values calculated from the above equations are listed in Table 1.

3.3. Infrared and Raman measurements

To shed more light on the infrared and Raman analysis of $A^{2+}B_2O_4$ (B = Fe, A = Cr, Mn, Zn, Ni, Fe) it is worth to mention that such phase crystallizes in a spinel structure of space group *Fd*-3*m*. Here, the factor group analysis predicts five Raman active modes namely A_{1g}+ E_g+ $3F_{2g}$ and 4 infrared active modes so-called $4F_{1u}$ [94]. The spinel $A^{2+}B_2O_4$ structure is usually characterized by two different structural subunits which are represented by tetrahedrally (A^{2+}) and octahedrally (B) ion coordination. Here, one can suppose that structure of various metallic spinel is closely related to each other. However, small differences are appearing at the moment of the isomorphic substitution between atoms which imply to the ideal distortion-free structure, point defects, activate additional bands and shift of another one towards higher and lower wavenumbers. Such defects are usually associated with: a) changes of the bond length, b) various ionic radii, c) incomplete occupancy of individual ion site or d) different valence of the ions. As a result, some bands might represent the vibration within only B-site and the other ones due to the presence of metallic modifiers in the unit cell originated from the mixed-type vibration of B-site and A^{2+} ions.

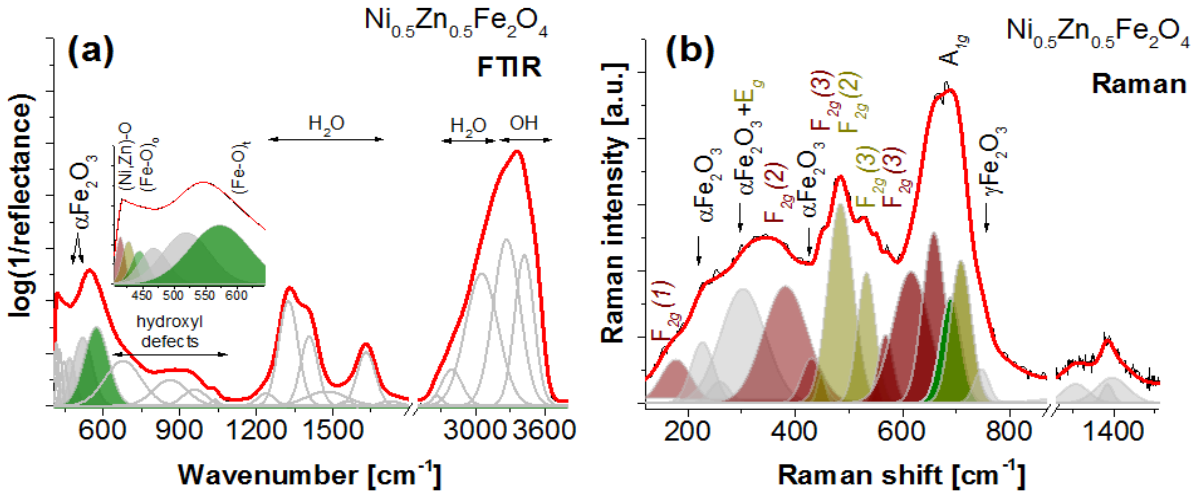

Figure 3. (a) FTIR and (b) Raman spectra of $Ni_{0.5}Zn_{0.5}Fe_2O_4$ nanoparticles. The characteristic bands originated from vibrational modes of main structural units were color-highlighted to better illustrate the structure of analyzed spinel. Additionally, co-associated iron oxide (hematite and maghemite phases were arrows-highlighted).

In such context, the infrared spectrum of nickel zinc ferrite nanoparticles illustrated in Figure 3a. In the region below 650 cm^{-1}, one can observe few overlapping bands originated

from the unit's vibration of spinel ferrite [56] as well as co-associated iron oxides. Hence, one can find bands located around 586 cm^{-1} and 425, 413 cm^{-1} associated with respectively ν_1 and ν_2 modes of tetrahedrally and octahedrally coordinated iron (Fe^{3+}-O), respectively. The position of such bands is determined by the presence of metallic modified e.g. nickel and zinc which provide a shift of the ν_1 band towards lower wavenumber and ν_2 towards higher wavenumber in relation to typical spinel ferrite [56,78,90]. The band shift is usually determined by isomorphic substitution of iron by a divalent modifier and lead to alteration of Fe-O bond length in depending on the iron coordination. Hence, the high-wavenumber band might evidence on magnetite while two low-lying bands at 425 and 413 cm^{-1} are linked, respectively to the occupancy of iron position by nickel (ν_2(Fe,Ni)-O) or zinc (ν_2(Fe,Zn)-O). A similar situation was also found in case of spinel ferrite with copper ions occupied the octahedral site in the crystal structure [57]. Other symmetrical modes usually correspond to the low-lying bands (<400 cm^{-1}) and there were not found on the analyzed spectrum. In turns, three bands at 445, 463, 517 cm^{-1} corresponds to the ν_2 (Fe-O) of low crystallize protohematite and might evidence of structural inhomogeneity of such phase [95]. Interesting is that on the infrared spectrum of spinel ferrite one can observe a lot of bands linked to the molecular water and hydroxyl units. It is especially well visible due to a strong signal in the region 1200 - 1600 cm^{-1} and 2550 - 3500 cm^{-1} originated, respectively from deformational modes as well as symmetric and asymmetric stretching vibration of water due to the unsaturated surface Fe atoms [96]. In addition, the region above 3500 cm^{-1} is characterized by bands linked to the hydroxyl units vibrational modes. Some explanation of the hydroxyl bands on the spectrum of spinel ferrite could be presence ferrihydrite [97–99] or water-soluble ferric (hydr)oxide [98,100]which are characterized through bands observed at 415–445 cm^{-1}. Moreover, according toliterature the origin of bands above 650 cm^{-1} have various explanations. Some of them ascribe to band at about 673 cm^{-1}corresponding to the presence ofa poorly-crystalline iron hydroxides such as

ferrihydrite [98,99,101–103], schwertmannite [104], akaganeite [101,105,106], amorphous goethite [106], Fe(III) oxy-hydroxides [98], hydromaghemite [107], and defective hematite (proto/hydrohematite) [108,109]. Another explanation for the origin of this band might be the bending mode of hydroxyl/water impurities adsorbed on the surface of hematite, or structurally incorporated into the structure of hematite or spinel ferrite [110]. In turns, bands at 846, 950, 1039 cm^{-1} might evidence of deformation vibrations of lattice hydroxyl ‘‘defects’’ localized at octahedral iron vacancies or δ(OH) mode of terminal hydroxyl groups (Fe-OH) on the hematite surface or within theoctahedrally coordinated iron site in spinel ferrite [95].

The number of Raman bands after peak fitting process observed in the spectrum of $Ni_{0.5}Zn_{0.5}Fe_2O_4$ exceeds from the one side, the band number expected for a normal spinel structure and from the other ones indicates the presence of co-associated iron oxides (see Figure 3b). Hence, in the 600 - 720 cm^{-1} range one can distinguish the A_{1g} symmetrical stretching modes of tetrahedral A^{2+}-O_4 (A = Ni, Zn, Fe). In addition, the number and position of bands of this region strongly depend on the type of cation (A^{2+}) occupying the tetrahedral position. As a result, in the A_{1g} mode region one can distinguish three bands centered at 658, 689, and 708 cm^{-1} characteristics, respectively for $\upsilon(ZnO)_4$, $\upsilon(FeO)_4$, $\upsilon(NiO)_4$. Moreover, the Raman band position in $Ni_{0.5}Zn_{0.5}Fe_2O_4$ spinel is in good agreement with data obtained for similar phases reported earlier [58,86,111,112]. In turns, the position of the tetrahedrally coordinated iron band indicates on magnetite [81]in the system while a broadband around 735 cm^{-1} to maghemite due to oscillations of Fe-O in uncompleted tetrahedrons with oxygen vacancies [113]. In addition, integrating the intensity of the thecertain component of A_{1g} mode give an opportunity to estimate the contribution of the corresponding cations to the tetrahedral sites using the theempirical formula given by *Lazarevic et al.* in form of $x_M(A) = I_M/(I_{Zn} + I_{Ni} + I_{Fe} + I_{Fe*})$ [58]. Here, one can assume that contribution of maghemite (I_{Fe*}) might be neglected because of the small share of this phase in relation to the other ones. Hence, such approximation leads to real

occupancy of the tetrahedral site in analyzed spinel as $Zn_{0.43}Ni_{0.33}Fe_{0.24}$. Furthermore, the position of A_{1g} bands is only slight blue-shifted in relation to pure spinel ferrites probably due to random occupancy of Zn and Ni in the various crystallographic sites [86,112]. It results from the appearance of vacancies which imply ion charge reduction of octahedral sites and lead to the local atom rearrangement [114]. Low-lying bands with F_{2g} symmetry are in turns, resulting from the vibrational modes within octahedral ion coordination. Here, one can assign to band centered at 384, 482 cm^{-1}, the asymmetric stretching F_{2g} (2) modes of Zn-O and Ni-O while to three bands located at 447, 530 and 563 cm^{-1} the asymmetric bending F_{2g} (3) modes of Zn-O and Ni-O (see Figure 3b). Unfortunately, E_g and F_{1g} (1) modes of Ni-component are overlapping with hematite-like bands [58], while F_{1g} (1) modes of Zn-component occurs in form of an alow intense band at 159 cm^{-1} [17]. A group of low intense bands above 1000 cm^{-1} is describing in literature as the interaction of electronic and magnetic levels with incident light and there are typically found in iron oxide phases such like hematite, magnetite, maghemite etc. [115].

3.4. Microstructure

Figure 4 represents the microstructure of $Ni_{0.5}Zn_{0.5}Fe_2O_4$ powder tested by the use of SEM microscopy. As one may notice there are predominantly visible particles mostly regularly shaped with diameters less than 100 nm. The reason of agglomeration in the synthesized nanoparticles may be attributed to the magnetic dipole-dipole interaction between nanoparticles. A similar behavior was also reported for various types of SF - NPs [61,62,116]. The detailed microstructural analysis was carried out by the use of TEM microscopy.

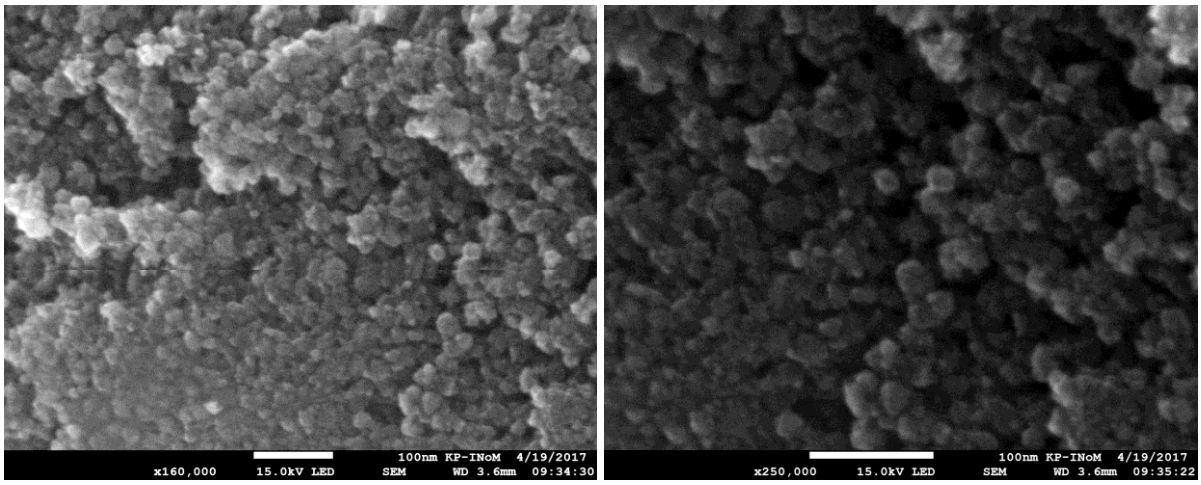

Figure 4. SEM images for the $Ni_{0.5}Zn_{0.5}Fe_2O_4$ particles.

The TEM micrographs of $Ni_{0.5}Zn_{0.5}Fe_2O_4$particles a represented in Figure 5. The first analyzed TEM image acquired in bright field (BF) (see Figure 5a) displays a group of agglomerated particles. The crystallites statistical distribution (CSD) of about 200 grains was estimated based on dark field (DF) image (see Figure 5b).

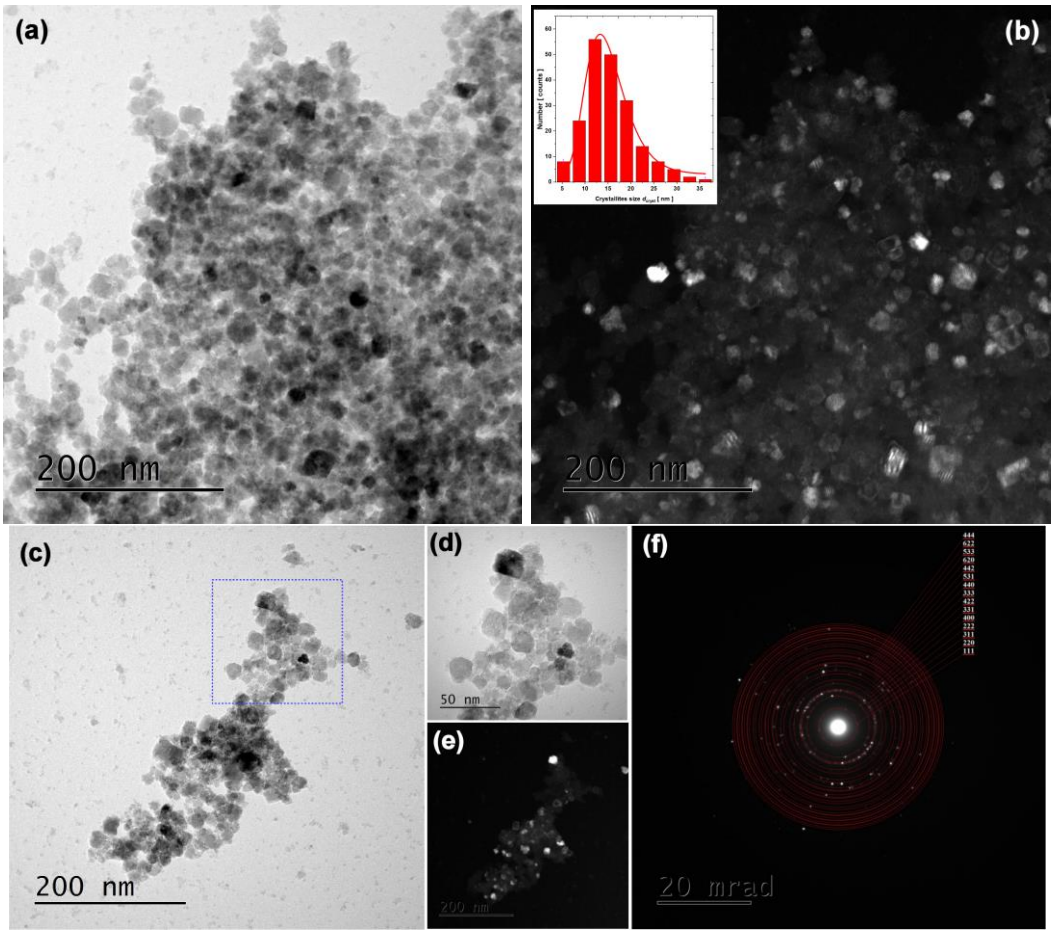

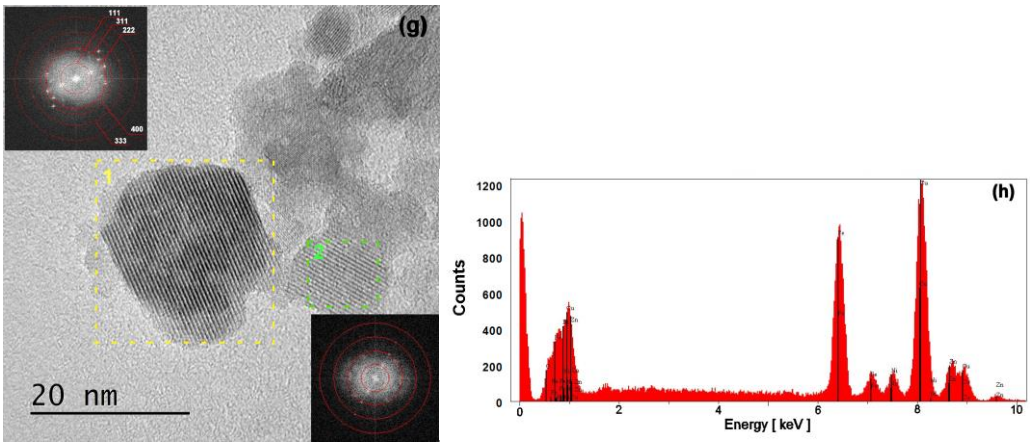

Figure 5. TEM micrographs for group of $Ni_{0.5}Zn_{0.5}Fe_2O_4$ particles, (a) bright field image; (b) dark field image with crystallites size distribution (CSD) as an upper left corner insert;(c) bright filed image taken for another part of sample; (d) magnification of the marked upper part; (e) dark filed image and corresponding (f) SAED pattern; (g) HRTEM image where upper and bottom inserts represents FFT images taken from a marked crystallites respectively; (h) EDS analysis performed for region of interest depicted in (c) image.

The corresponding crystallites size distribution (CSD) histogram placed as an insert into Figure 5b was fitted with the use of the following statistical log-normal function [6]:

$$P(D) = \frac{A}{D\,\sigma_D\sqrt{2\pi}} \exp\left[-\frac{1}{2\sigma_D^2}\ln\left(\frac{D}{d_{cryst}}\right)^2\right] \qquad (12)$$

where σ_D denotes the standard deviation of the average crystallites size d_{cryst} which equals d_{cryst} ~ 14.78nm ± 2.56 nm with the minimum size of 5.27 nm and maximum size of 39.65 nm. The second TEM region of interest (see Figure 5c-e) image reveals a small number of agglomerated SF - NPs, for which the selected area electron diffraction pattern (SAED) was recorded (see Figure 5d). Its analysis confirms the presence of the inverse ferrite spinel structure typical for the $Ni_{0.5}Zn_{0.5}Fe_2O_4$ phase. The diffraction lines clearly indicate the nanoscale crystallinity of the particles with randomly oriented polycrystalline symmetry.

The AFM topography of the $Ni_{0.5}Zn_{0.5}Fe_2O_4$ particles revealed the distribution of rather regular particles/grains placed on flat mica substrate (see Figure 6). The statistical analysis was started by marking the grains by the grain segmentation method implemented in Gwyddion software [117]. The marking parameters were adjusted for the correct marking of the visible grains. Due to its semi-automatic character, this method provides a satisfactory estimation, rather than absolute value of a particles/grain sizes. As a consequence, a histogram with

'equivalent radius' of a grain (r_{eq}) is provided. The r_{eq} value is obtained by taking the area of each masked grain and calculating the radius of a circle with the same area as the grain. This allows for the reliable comparison of different grains aside from their shape. The obtained distribution of about 208 particles revealed the value of r_{eq} values estimated by using the statistical log-normal function equals about 9.34 nm (see the bottom right panel in Figure 6). Thus, the average particles size defined as a diameter i.e. doubled r_{eq} value estimated based on AFM analysis is in the range of about 18.68 nm ± 0.19 nm, which is close to XRD and TEM estimation.

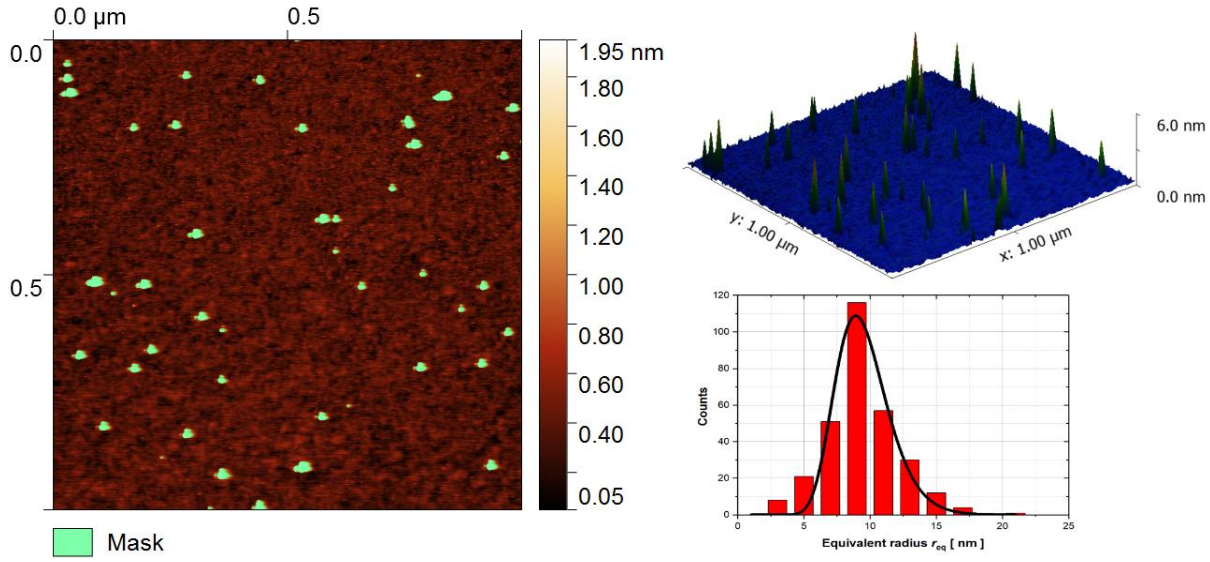

Figure 6. The left panel - 2D AFM topography. Green dots represent $Ni_{0.5}Zn_{0.5}Fe_2O_4$ particles. The upper right panel - the 3D representation. The bottom right panel is the histogram distribution of r_{eq} values.

The visible slight discrepancies between crystallites size estimated from XRD, TEM and AFM investigations are probably related to the irregular shapes of nanoparticles. Nonetheless, the agglomeration process confirmed by DLS and SEM studies and the structural disorder and/or amorphousness at the surface may also influence the visible mismatch in d_{cryst} values. For further analysis, the d_{cryst} value from TEM method was taking into account.

3.5. XPS measurements

First of all the XPS analysis was carried out in order to estimate the presence of each element in the formula and to verify its oxidation chemical state. Such analysis is done for the $Ni_{0.5}Zn_{0.5}Fe_2O_4$ system for the first time. The XPS survey spectra for the $Ni_{0.5}Zn_{0.5}Fe_2O_4$ sample collected after various ion treatment were illustrated in Figure 7a . The main photoemission peaks Zn2*p*, Fe2*p*, O1*s*, C1sare identified in the measured spectra. The Ni2*p* states are overlapped with the Auger Fe LMM lines and are barely visible even after 45 min of ion cleaning. It is worth adding, that there are no additional impurities besides C1*s*, which can be mainly treated as the surface impurity. The detailed analysis of the valence band spectra (right upper panel) over etching procedure exhibits the visible separation of Zn3*d* states (BE ≈ 7.5 ÷ 11.3 eV) overlapped with hybridized Ni3*d*/Fe3*d* bands.

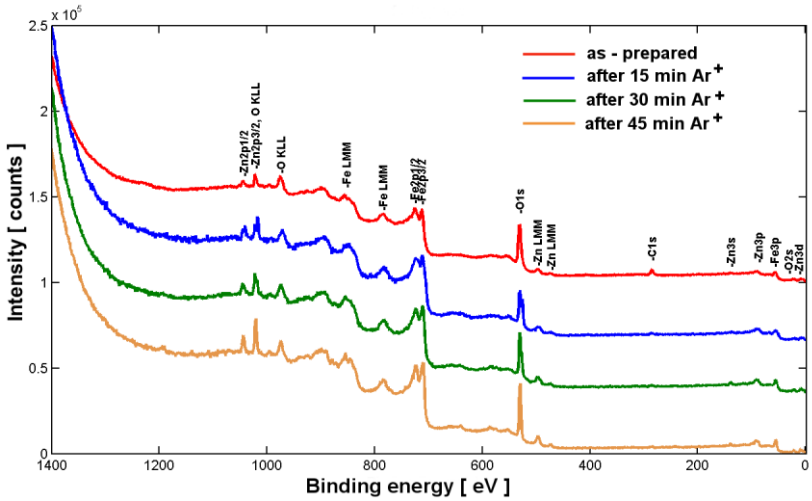

Figure 7 (a). XPS survey spectra for the$Ni_{0.5}Zn_{0.5}Fe_2O_4$ nano ferrites acquired after various surface treatment.

Figure 7b represents the evolution of individual core level lines over applied ion etching procedure. The broadening of photoemission peaks at the beginning of measurements is related to the surface impurities. Therefore for further analysis and detailed identification of the oxidation state of elements the last obtained spectra namely after 45 min of Ar^+ beam cleaning were processed. Similarly, the estimation of the elemental ratio (Ni,Zn)/Fe/O in the tested sample was performed after the last step of cleaning pointing to the elemental quantity: C1*s* – 5.4 at %, N1*s* – 4.0 at %, O1*s* – 58.0 at %, Fe2$p_{3/2}$ – 17.7 at %, Ni2$p_{3/2}$ – 7.1 at % and Zn2$p_{3/2}$–

7.7 at %. Thus, we may infer that generally the expected stoichiometric ratio is retained. However, small discrepancies between theoretical and experimental 1/2/4 ratio may be attributed to overlapping of Fe2*p* and Ni Auger lines.

The evolution of Zn2*p* lines split into $2p_{3/2}$ and $2p_{1/2}$ reveals the separation and appearing of double peaks for each 2*p* lines. Thus, that one with lower BE may be ascribed as pure Zn metal whereas, that located at higher BE and having higher intensity is rather typical for ZnO states. The value of LS splitting is about $\Delta E \approx 23$ eV. We do not present Ni2*p* line, which is overlapped with Fe LMM Auger lines giving a broad structure with relatively low intensity. The iron Fe2*p* lines depicted in the middle bottom panel due to spin-orbital coupling interactions between the 2*p* core hole and unpaired 3d electrons split into two components namely Fe$2p_{3/2}$ and Fe$2p_{1/2}$ with an LS splitting of about $\Delta E \approx 13.34$ eV. Both lines are composed of several species due to various iron chemical states, especially a visible shoulder at lower binding energy range after 30 min and 45 min of Ar^+ etching may be attributed to pure iron metallic states.

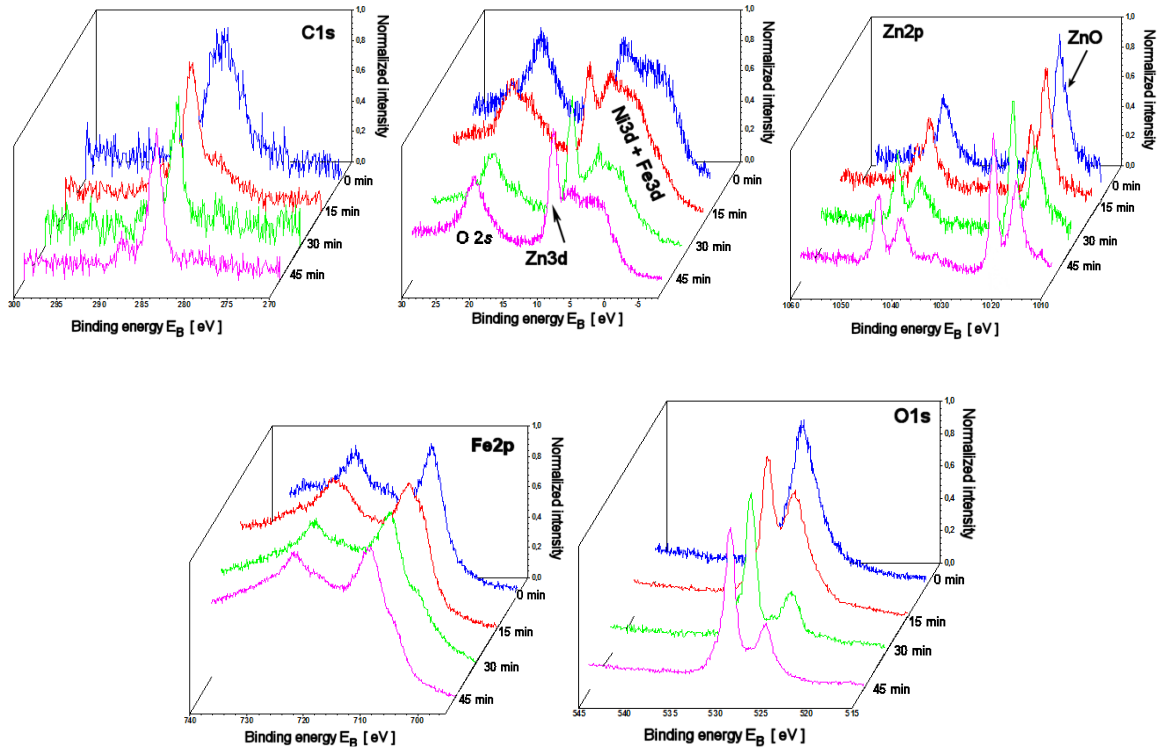

Figure 7 (b). XPS core level lines for the$Ni_{0.5}Zn_{0.5}Fe_2O_4$ nano ferrites acquired after various surface treatment.

As we mentioned previously for further detailed analysis we select the Fe2*p* line after 45 min. of ion cleaning. High-resolution core-level XPS spectra fitted after 45 min of ion cleaning are depicted in Figure 7c. The deconvolution parameters obtained by the fitting procedure with the use of Shirley background and Lorentzian - Gaussian shape of photoemission lines are listed in Table 2.

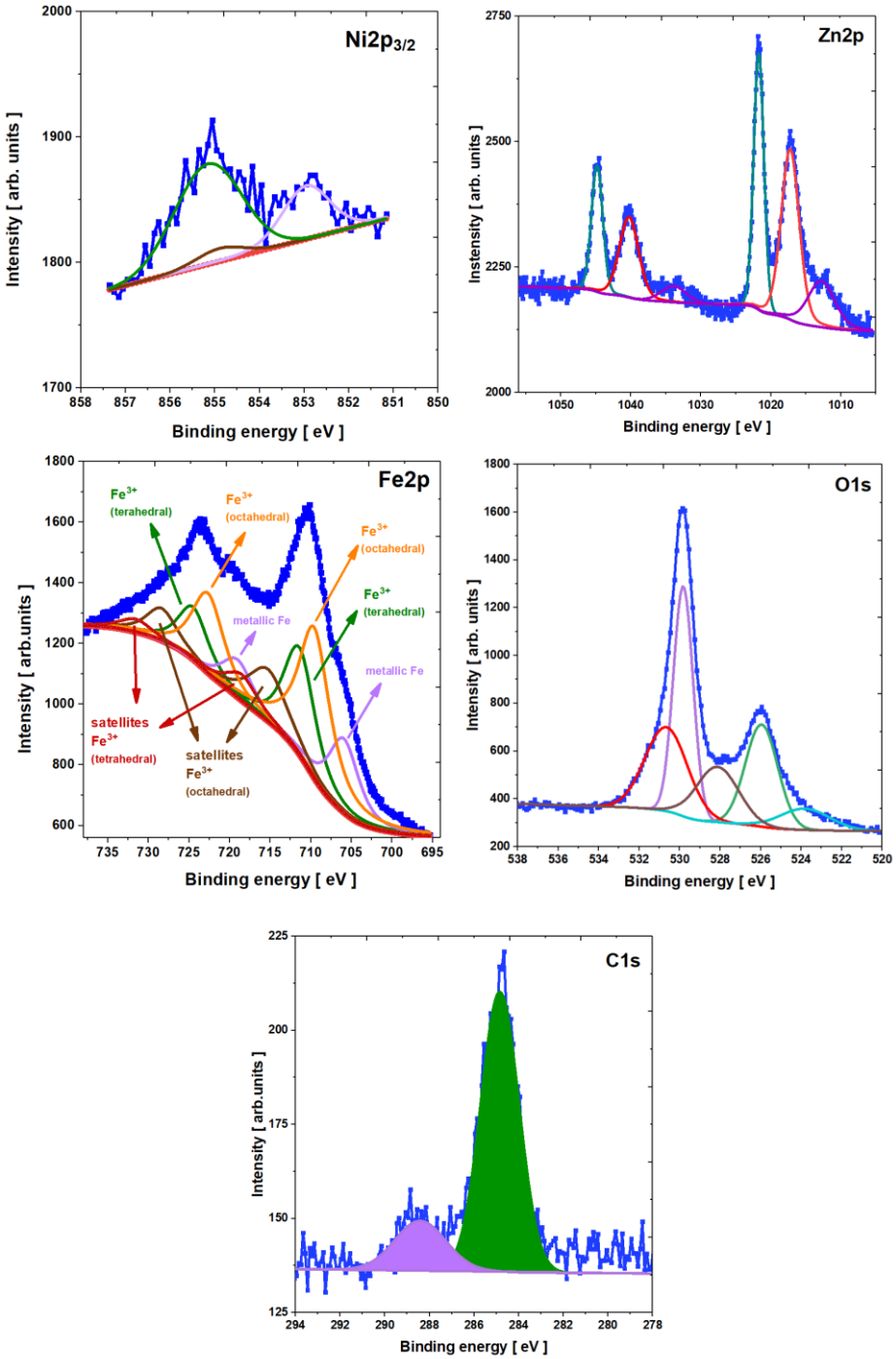

Figure 7(c). XPS core level lines spectra for the$Ni_{0.5}Zn_{0.5}Fe_2O_4$ nano ferrites deconvoluted after 45 min of argon etching.

The deconvolution of Ni2*p* core level reveals the existence of three peaks at 852.96, 854.89 and 855.15 eV. The first two may be assigned as typical for metallic nickel – the main photoemission Ni2$p_{3/2}$ line and its satellite. The last one is rather for Ni^{2+} states in B – octahedral or typical for NiO states. It is well known, that XPS measurements performed for nanoparticles

reveals their oxidation [70]. For the Zn2*p* spectrum, peaks fitted at 1012.8 and 1033.9 eV maybe are related to Zn2$p_{3/2}$ and Zn2$p_{1/2}$ respectively, for pure metallic zinc. The peaks at 1017.2 and 1040.3 eV are rather typical for Zn^{2+} states belonging to ZnO, whereas those at 1021.7 and 1044.8 eV corresponds tetrahedrally coordinated divalent zinc ions located at A – site in a spinel structure, similarly as in $ZnFe_2O_4$[83,84]. There is rather no evidence of migration of zinc ions into an octahedral site like in $ZnFe_2O_4$ ferrites synthesized by mechanochemical routes, where the zinc cations are randomly distributed on the surface [84,85].

The O1*s* line is more complex and after deconvolution with Gaussian peaks exhibits five components due to various oxides states but also to surface impurity. Simultaneously as for other spinel ferrites [61] the peak around 528 eV may be related to double metal cation bonding Fe = O, while that around 530 eV probably to Fe – OOH [87] or to covalent bonds between two atoms and/or oxygen Fe – O – Fe, Ni/Zn – O – Ni/Zn, Fe – O – Ni/Zn [61]. Nonetheless, the complexity of O1s line especially at low binding energy range may arise from various surface layer structure and interior of particles. The analysis of Fe2*p* lines reveals the presence of ten components related to various iron species. The 2p line typical for pure metallic iron is fitted with two peaks splitted into Fe2$p_{3/2}$ (BE = 705.92 eV) and Fe2$p_{1/2}$ (BE = 719.02 eV). The dominated doublet Fe2$p_{3/2}$ (BE = 709.57 eV) and Fe2$p_{1/2}$ (BE = 722.67 eV) broad lines may be assigned to iron states characteristic for Fe^{3+} ions simultaneously in B -octahedral sites. Such lines are accompanied by satellite shake-up peaks around 5.7 eV above main B - site line. Meanwhile, the presence of the peaks around 715.29 eV and 724.50 eV and simultaneously satellites around 718.51 eV and 731.61 eV may indicate the existence of Fe^{3+} species in more than B – site and corresponds to A – tetrahedral site. The performed deconvolution of Fe2*p* lines confirms the inverse spinel structure. Such behavior was already observed in photoemission studies for other nanoparticles [71,82]. It is in agreement with XRD refinement, where iron 3+ ion was evidenced in two sites: B – octahedral and A – tetrahedral.

However, the peak positions of both Fe2$p_{3/2}$ and Fe2$p_{1/2}$ lines corresponding to B – sites and their satellites coincide with the peaks positions of Fe^{2+}. Thus, the occupation of the octahedral B – site by Fe^{3+} and Fe^{2+} cations is not excluded [61,63,72] but was not confirmed by XRD experiment. Taking into account the main peak of Fe^{3+} for B – site and simultaneously for A – site as well as their satellite lines for the Fe2$p_{3/2}$ spectra the Fe^{3+}(A)/Fe^{3+}(B) ratio is estimated as 0.57 which is close to the results of XRD refinement.

Table 2. Results of deconvolution of XPS core level lines after 45 min. of Ar^+ ion etching for the $Ni_{0.5}Zn_{0.5}Fe_2O_4$ spinel nano ferrites.

Line	Binding energy [eV]	Separation [eV]	Area [%]	FWHM	Gauss [%]	χ - Squared
Fe2p	705.92	0.00	10.85	4.41	36	2.27
	709.57	3.65	25.37	4.67	12	
	711.40	5.48	16.17	4.56	37	
	715.29	9.37	10.12	5.68	27	
	718.51	12.59	4.16	4.61	27	
	719.02	13.10	5.43	4.50	47	
	722.67	16.75	12.68	4.67	29	
	724.50	18.58	8.08	4.48	27	
	728.39	22.47	5.06	4.53	27	
	731.61	25.69	2.08	4.61	27	
Ni2p3/2	852.96	0.00	27.22	1.25	62	1.01
	854.89	1.94	6.39	1.25	90	
	855.15	2.20	66.39	1.78	100	
Zn2p	1012.8	0.00	12.93	4.57	70	1.43
	1017.2	4.45	30.25	3.03	80	
	1021.7	8.94	24.15	1.72	95	
	1033.9	21.06	3.90	4.30	90	
	1040.3	27.47	15.30	3.25	80	
	1044.8	32.02	13.48	1.90	89	
O1s	523.8	0.00	7.19	2.92	100	1.46
	525.9	2.13	22.32	1.88	100	
	528.1	4.31	15.74	2.45	100	
	529.8	6.00	30.53	1.14	100	
	530.6	6.83	24.22	2.48	100	
C1s	284.8	0.00	81.09	2.01	100	1.66
	288.4	3.57	18.91	2.67	100	

The discrepancy between XPS and XRD may be due to the different sensitivity of both techniques. The XPS is surface sensitive technique and it provides the chemical information

from the top of atomic layers, whereas XRD is rather a the bulk method. The chemical composition of the synthesized ferrite is also modified by the applied ion etching and after 45 min of Ar^+ sputtering the XPS measurements reflect not only the structure of the near-surface layers but also the disorder in the interior of studied nanoparticles. Thus, the observed various zinc, nickel and iron species may be caused by different atomic configurations in the interface/surface regions of particles and their interior. It seems that all oxides are accumulated on the surface/interface regions, whereas are cations distribution typical for inverse spinel structure is rather visible in the interior of particles. The observed contributions from pure metallic Zn and Fe may be assigned to the small metallic clusters, probably present in the core of nanoparticles, while their surface layer is dominated by oxides. The C1s spectrum reveals two species. The first one at 284.8 eV, which dominates is related to the carbon accumulated on the surface whereas the second around 288.4 eV may be ascribed as various carbonates.

3.7. Magnetic measurements

The magnetic measurements of $Ni_{0.5}Zn_{0.5}Fe_2O_4$ nano ferrites were made using SQUID magnetometer. Figure 10 shows typical magnetic hysteresis (M-H) loops collected at three different temperatures: 2 K, 100 K and 300 K. The estimated magnetic parameters such as saturation magnetization (M_S), remanence magnetization (M_R) and coercivity (H_C) are placed in Table 3. It is worth noticing, that the measured hysteresis loops exhibit typical for spinel ferrite a thick S-shape [61]. However, at low temperature, these nanoparticles exhibit rather the ferromagnetic nature whereas for $T \geq 100K$, the possible existence of superparamagnetic (SPM) behavior may occur, which is confirmed by almost zero coercivity and almost negligible remanence (see Figure 8a and Table 3). Since the coercivity is the measure of the magnetocrystalline anisotropy small particles with zero hysteresis loop exhibit low anisotropy and they are unblocked. Furthermore, at higher temperatures the thermal energy overcome the anisotropy energy leading to zero value of coercivity. Previously, for the same Zn content the

small value of H_C at room temperature (200 gauss) was explained as the ferromagnetic behavior probably due to quite a large crystallite size (16.76 nm) comparing to other Zn doping for which coercivity vanishes [30]. Nonetheless, the SPM state was evidence in $Ni_{0.5}Zn_{0.5}Fe_2O_4$ by analyzing the Mössbauer spectra recorded at the room temperature, which revealed the paramagnetic doublet typical for Fe^{3+} occupying the octahedral site [46].

The non-saturated hysteretic behavior in Zn – based ferrites may suggest the possible existence of strong inter-cluster antiferromagnetic interactions mixed with the ferromagnetic ones inside clusters [20]. The non-saturated magnetization even at high applied external magnetic field can be also related to the presence of small nanoparticles having a core-shell like morphology, with ferrimagnetically arranged core and spin-glass-like surface layer. In another case, the lack of outer surface layer would be manifested by the saturation of magnetization. So, the influence of dipolar interaction and surface anisotropy may have an impact on non-saturated hysteresis. A similar scenario can be realized in the case of studied $Ni_{0.5}Zn_{0.5}Fe_2O_4$ nano-ferrite. Here, one may also notice non-saturated hysteresis loops. So in order to obtain the saturation magnetic moment M_S we applied the extrapolation to the infinite field.

Generally, magnetic nature of ferrites is dependent on the method of their synthesis, the distribution of cations between the interstitial tetrahedral and octahedral sites but also on the microstructure and the particles size. It is worth noticing, that the introduction of an-magneticZn^{2+} ions into $NiFe_2O_4$ results in the migration of Fe^{3+} ions from A to B-sites, which causes the increase the of the B-site magnetic moment and consequently increases the total magnetization. So, for spinel ferrites, especially based on $Ni_{1-x}Zn_xFe_2O_4$ [1,2,18–32,34–54,56–59,89] the magnetization may be explained by the two – sublattice Néel's model [1,19,50] based on A and B magnetic sublattices having oppositely aligned magnetic moments coupled with super-exchange interactions related to cations distribution on A and B sites. Therefore the magnetic moment expressed in μ_B per formula unit [μ_B/f.u] may be calculated as:

$$m_B\left(theor\right) = M_B - M_A \qquad (13)$$

where M_B and $M_A$denote magnetic moments in B and A sites respectively. The values of m_B can be estimated based on cations distribution obtained from XRD refinement and by taking into account the values of ionic-magnetic moments (Ni^{2+} - $2\mu_B$, Zn^{2+} - 0 μ_B, Fe^{3+} - $5\mu_B$). The calculated value (m_B (*theor*) = 6 μ_B) may be compared with experimentally obtained from $M(H)$ curves at the room temperature (m_B = 1.93 μ_B) or at 2 K (m_B = 3.43 μ_B). The large difference may arise from the surface spin disorder, spin canting effect or spin-glass-like state due to local chemical disorder, broken exchange interactions and various local symmetry for atoms near the surface region as it was previously evidenced in other Zn - doped nickel ferrites [46,72]. It may be explained by *Yafet – Kittel* [79,118] on the basis of three sublattice model. According to such approach, the B – magnetic sublattice is composed of two B1 and B2 sublattices, which form the triangular lattice. Each of them has the equal in magnitude but oppositely canted magnetic moments with the canting angle denoted as α_{YK}. The value of α_{YK} angle may be calculated based on the equation:

$$m_B\left(exp\right) = M_B \cos\alpha_{YK} - M_A \qquad (14)$$

where $m_B(exp)$ is the experimental value of saturation magnetization at 300 K expressed in [μ_B/f.u]. The estimated value of canting angle equals $\alpha_{YK} \approx 58.6°$, which is close to the value 53.64° for $Ni_{0.6}Zn_{0.4}Fe_2O_4$ [32] and between values 43.46° and 62.52° previously calculated respectively for x = 0.4 and 0.6 zinc content in $Zn_xCo_{1-x}Fe_2O_4$ [79]. The larger value of α_{YK} points to an anon-collinear structure of B – sites, which may strengthen B – B interactions and simultaneously leads to weakening of A – B interactions confirmed by the large discrepancy between $m_B(exp)$ and $m_B(theor)$ values. So, one may infer, that in studied systems B – canted spin structure dominates at the surface.

Thus, for the case of $Ni_{1-x}Zn_xFe_2O_4$ system [1,2,18–32,34–54,56–59,89], where the inverse spinel structure is present the Ni^{2+} ions are preferentially located at B - octahedral site,

whereas Fe^{3+} is uniformly distributed at A- tetrahedral and B - octahedral sites. The Zn^{2+}, which is rather non-magnetic, nominally substituted in place of 50% of Ni^{2+}preferentially is distributed over A- tetrahedral site forcing some of the Fe^{3+} ions for transferring to B - octahedral site. Thus, as a consequence the A – site magnetization decreases the overall magnetic parameters for the $Ni_{1-x}Zn_xFe_2O_4$ usually are reduced over Zn doping [30,31]. The remanent magnetization and the saturation magnetization are influenced by the magnetic exchange between A and B site but also by the different arrangement of magnetic moments on the surface and in the interior of particles. The squareness of the hysteresis loop known as M_R/M_S ratio is lower than the value of 0.5 predicted by the Stoner–Wohlfarth (S–W) model for randomly oriented single domains nanoparticles [119]. The M_R/M_S dependence is sensitive to particles/crystallites size as well as the variation of anisotropy induced by an external magnetic field and in real compounds its value predicted by the S–W model is mostly different than 0.5 due to magnetic interactions. In our case, such ratio is probably related to the influence of the uniaxial anisotropy as for particles which exhibit superparamagnetic behavior. The value of M_S may be affected by the different magnetization process in the core and on the surface of particles due to possible surface spin disorder. Thus, the significant reduction of M_S value for nanosized Zn – based ferrites compared to their bulk parent compound [120] is a consequence of various magnetic state at the surface of NPs due to surface spin disorder state.

In our case, the obtained values of magnetic parameters are in good agreement with previously evidenced for the same kind of compounds [1,2,18–32,34–54,56–59,89], but we have to be aware that the observed small discrepancies may be caused by the particles size dependent on the type of synthesis method [10].

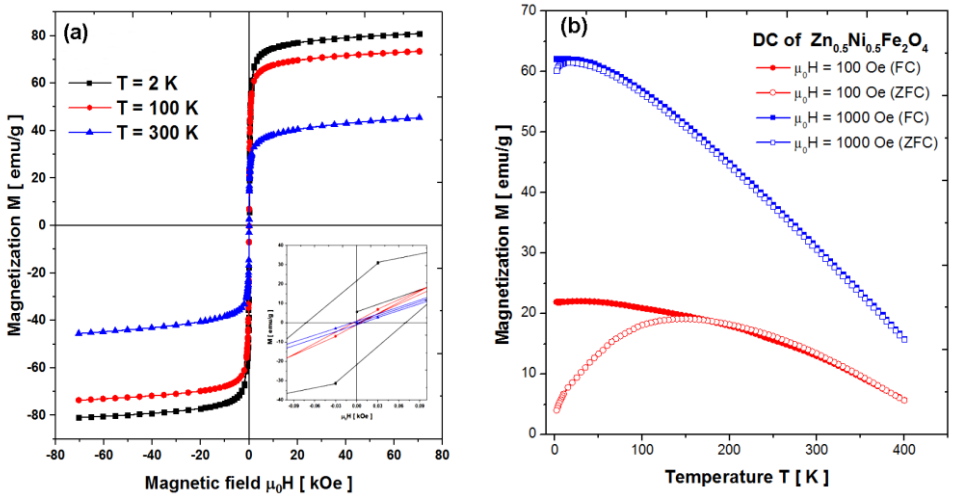

Figure 8. (a) Hysteresis loops at 2K,100K, and 300K. The inset represents the magnification of all loops. (b) DC magnetization at 100 Oe and 1000 Oe for the $Ni_{0.5}Zn_{0.5}Fe_2O_4$ spinel ferrites.

The average value of crystallites size determined from TEM measurements is about d_{cryst} ~ 14.2 nm ± 4.2 nm. The critical size of magnetic domains in such particles, which can be useful to determine the SPM behavior of an assembly of single-domains of particles is unknown. However, almost zero value of room temperature coercivity estimated from M(H) loops does not exclude the SPM behavior. Therefore, in order to characterize the magnetic behavior of such particles in details DC and AC magnetic measurements were carried out.

The DC magnetization measured at zero fields cooled (ZFC), field cooled (FC) modes and at the external magnetic field of 100 Oe and 1000 Oe summarized in Figure 8. For the M_{ZFC} versus T curve measured at H_{appl} = 100 Oe a broad maximum at T_{max}≈ 150 K ± 5 K is observed, which is related to the blocking of particles which takes place at a certain temperature namely the blocking temperature T_B. Here, the broad bump at T_{max} may rather suggest a distribution of blocking temperature, that is a distribution of particles size. It is worth mentioning, for an assembly of nanoparticles, the maximum at T_B is usually considered as a mean value of the temperature, at which the equilibrium between the thermal energy and magnetic anisotropy in the measurement process. Above T_B the M_{ZFC} magnetization decreases due to unblocking of the magnetic moments of smaller particles and it bifurcates with M_{FC} curve at the temperature of irreversibility (T_{irr}), which denotes the temperature of unblocking of larger

particles in the sample. The irreversibility related to the blocking process is also observed for H_{appl} = 1000 Oe, which is rather higher than the anisotropy field. A similar process was observed e.g. for $CoFe_2O_4$nanoferrites [63]. In the case of DC measurements for uniaxial particles the blocking temperature may be ascribed as:

$$T_B = \frac{K_{eff}V}{25k_B} = \frac{E_a}{25k_B} \qquad (15)$$

where $E_a = K_{eff}V$ denotes the effective anisotropy energy with the effective anisotropy constant K_{eff} and the volume of particle V, k_B is the Boltzmann constant. Taking into account the value of T_{max} from ZFC measurement and the average particles size from TEM one may estimate the value of E_a and subsequently the value of K_{eff} constant assuming that particles are spherical. Furthermore, one may estimate the value of critical particles diameter (D_{crit}), below which particles can be treated as a single domain by the following formula [23,66]:

$$D_{crit} = \frac{9E_p}{2\pi M_S^2} = \frac{9\sqrt{\frac{2k_BT_CK_V}{a}}}{2\pi M_S^2} \qquad (16)$$

where E_p denotes the energy density of the magnetic domain wall, M_S is the saturation magnetization, T_C is the Curie temperature estimated from the Faraday balance measurements T_C = 570 K ± 20 K, K_V is the magneto-crystalline anisotropy constant, and a is the lattice parameter. It is well known, that interactions between nanoparticles lead to increase of anisotropy expressed as effective anisotropy constant:

$$K_{eff} = K_V + K_{sh} + K_S + K_i \qquad (17)$$

where individual contributions reflect to shape anisotropy K_{sh}, surface anisotropy K_S, supplementary constant anisotropy related interactions K_i[23]. So, in calculations the value of the critical particles diameter we used the K_{eff} value estimated from magnetic measurements instead of K_V, which can increase the value of D_{crit}. The calculated value at the room

temperature equals $D_{crit} \approx 63.36$ nm, which is quite large comparing to the value of d_{cryst}. So, we may infer that studied SF – NPs exhibit the SPM behavior at 300 K.

The AC magnetic susceptibility measurements at various frequencies represent a very useful tool to study dynamical properties of magnetic nanoparticles. At T_B the relaxation time τ of non-interacting particles related to the average time between the reorientation of the magnetization direction, may be described by Néel –Arrhenius law:

$$\tau = \tau_0 \exp\left(\frac{\Delta E_a}{k_B T}\right) \qquad (18)$$

where ΔE_a denotes the magnetic anisotropy energy barrier to anisotropy energy required for reversal of magnetic moment orientation, which for uniaxial anisotropy is given as $\Delta E_a = KV$ with the effective magnetic anisotropy constant K_{eff} and the particle volume V; k_B is Boltzmann constant. The relaxation time is the inverse of measuring frequency ($\tau = 1/2\pi f$) and the τ_0 value for typical SPM particles is usually in the range of 10^{-9} – 10^{-13} s [1]. However for magnetic ferrofluids[1,63,66], where the weak inter-particle dipolar interactions are taken into account and describe the relaxation time of the particles in the vicinity of the temperature T_B is related to the Vogel- Fulcher (V-F) law:

$$\tau = \tau_0 \exp\left[\frac{\Delta E_a}{k_B (T_B - T_0)}\right] \qquad (19)$$

where T_0 is dependent on the particles interaction.

The existence of inter-particle interactions can be deduced from the analysis of the AC magnetization data. In Figure 9a and b are presented curves of the real χ' and imaginary χ'' parts of the AC magnetization measured at several frequencies between 1 and 100 Hz. As the temperature is increased, a cusp occurs in both susceptibilities, which may correspond to the transition from the blocked state to the superparamagnetic state (SPM), as expected for an assembly of single-domain particles. The maximum in the real component of χ' denoted as T_{max1} is shifted towards higher T with the increase of frequency. Similar behavior is observed for the

maximum visibility in the imaginary part of χ'' denoted as T_{max} (see Figure 9 and Table 3). This phenomenon is characteristic for spin glass states, but also for interacting or non-interacting nanoparticles. The values of T_{max1}, as well as T_{max2}, are significantly higher than T_{max} estimated from ZFC measurements. Nonetheless, its value is related to the average blocking temperature $T_{max} \sim \beta\langle T_B \rangle$, where the parameter β is dependent on the particle size distribution [65]. Thus, for monodispersed samples $\beta = 1$, whereas for particles size distribution such parameter is related to $g(D) = \delta(D - D_0)$ size distribution [121].

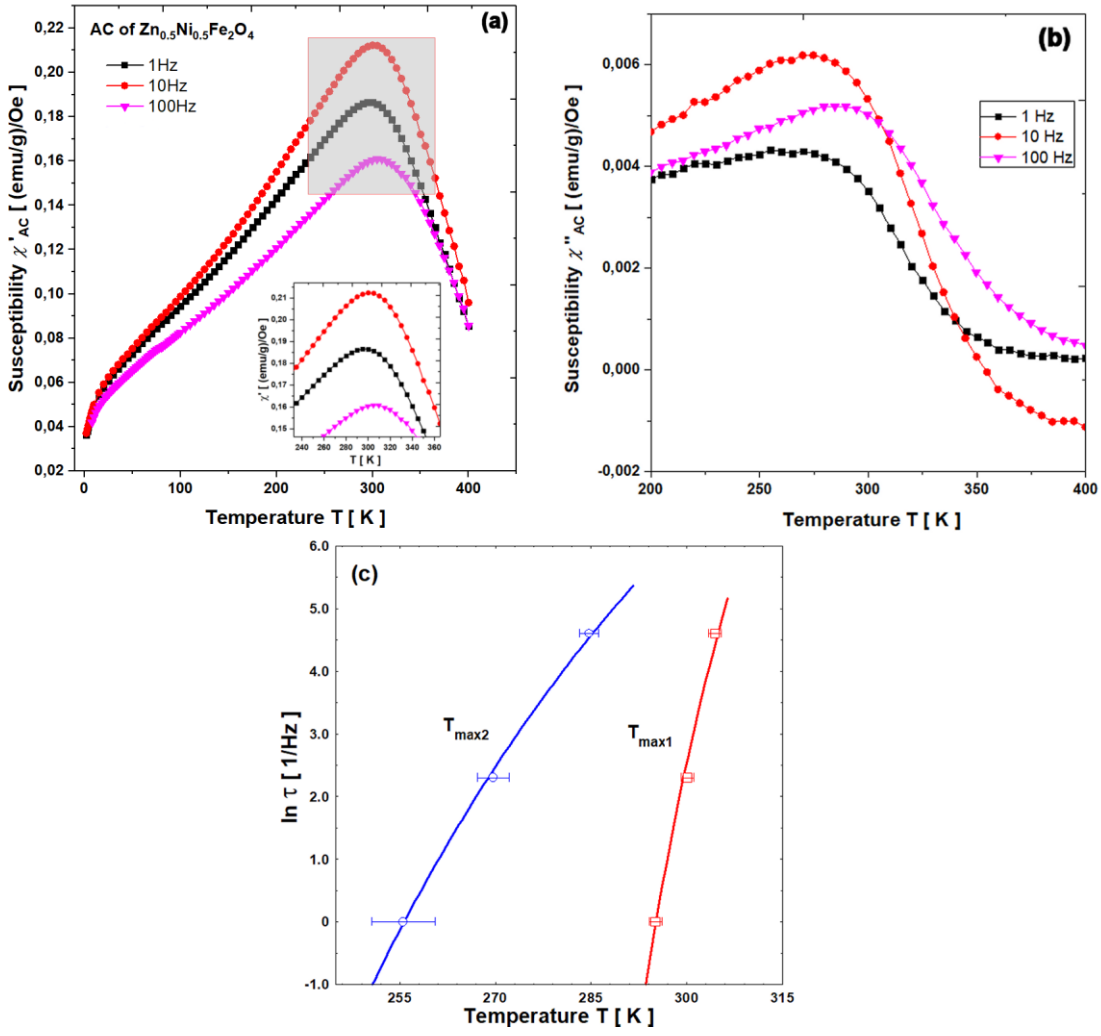

Figure 9. The temperature dependence of the (a) real χ' and (b) imaginary χ'' parts of AC magnetic susceptibility at 1 Hz, 10 Hz and 100 Hz in the $Ni_{0.5}Zn_{0.5}Fe_2O_4$ spinel ferrites. (c) Frequency-dependent temperature T_{max1} and T_{max2} estimated from a maximum in the real χ' and imaginary χ'' parts respectively. The solid curves represent fit of the Vogel-Fulcher law (19) to the experimental data.

So, the observed diversity in T_{max} estimated from AC measurements may be a consequence of relatively low polydispersity (PDI = 0.171 ± 0.011), but also may originate from two kinds of relaxation. Thus, below T_{max2} particles may be probably frozen and cannot move, and relaxation of the particles magnetic moments may occur relatively through the Néel relaxation. However, in the temperature range $T_{max2} < T < T_{max1}$ nanoparticles appear to be in a mixed state. The magnetic measurements were performed on the loosely packed powder and therefore probably in such conditions nanoparticles may be rather free to move locally. In the presence of the external magnetic field, such movement is related to the Brownian relaxation as a response to magnetic moments of loosely packed nanoparticles.

A reasonable quite good fit of the Vogel-Fulcher law to the experimental data ln τversus $T'_B = T_{max1}$ as well as $T_B = T_{max2}$ is obtained with physically meaningful parameters (see Figure 9c and Table 3). The best fit yields $\tau_0 = (5.1 \pm 0.5) \times 10^{-10}$ Hz, $\Delta E_a/k_B = (877 \pm 139.9)$ K and $T_0 = (255 \pm 2.6)$ K as well as $\tau'_0 = (1.43 \pm 0.2) \times 10^{-11}$ Hz, $\Delta E'_a/k_B = (2947 \pm 874.8)$ K and $T'_0 = (132 \pm 1.4)$ K for T_{max1} as well as T_{max2} respectively. The parameters estimated from the Vogel-Fulcher fitting describing the Néel relaxation (below T_{max2}) and the Brownian relaxation (below T_{max1}) point to much larger Brownian relaxation than Néel relaxation. The visible difference may be associated with the different nature of these two relaxations. It is interesting to note that, the value of T_0estimated from the Vogel - Fulcher expression is similar to $T_{max} = T_B$ estimated from DC measurements. Nonetheless, the discrepancy of T_{max} values obtained from AC and DC measurements is related to various τ_m, time measurement in agreement with formula (18) and (19) caused by the difference within measurement device.

Contributions to the effective activation energy barrier ΔE_a estimated based on obtained parameters can originate from intrinsic anisotropies of the particles like the influence of their shape, magneto-crystalline or stress anisotropies but also of the inter-particle dipolar or exchange interactions as well as the influence of the surface effects. The effective anisotropy

constant K_{eff} deduced from V-F fitting contains all above contributions. Its value was calculated based on the average crystallites size taken from TEM studies. Thus, the obtained value of K_{eff} is in reasonable agreement with previously reported for Ni – Zn ferrites [1,23,54]. However, it seems that anisotropy constant is dependent on the zinc concentration. As it was shown, the value of K_{eff} was reduced with the increase of Zn content pointing to the decrease of domains wall energy [1,50,59,79,118]. The value of critical domains size D_{crit} estimated based on AC parameters at T_{max2} and 300 K is in a quite good agreement with that one from DC measurement (see Table 3) indicating the Néel relaxation.

Table 3. Magnetic parameters for the $Ni_{0.5}Zn_{0.5}Fe_2O_4$ spinel nano ferrites.

Hysteresis loops				**DC measurements**				
	T = 2K	**T = 100K**	**T = 300K**	**T_{max} [K]**	150 ± 5	**E_p [erg/cm^2]**	24.45 ± 2.04 × 10^{-4}	
M_S [emu/g]	80.66	73.26	45.44	**V [nm^3]**	1615.33 ± 103.18	**D_{crit} [nm]**		
M_S [μ_B/f.u]	3.43	3.12	1.93	**K_{eff}× 10^5[erg/cm^3]**	3.204 ± 0.311	**T = 2K**	**T = 100K**	**T = 300K**
M_R [emu/g]	21.82	0.95	0.83					
H_C [kOe]	0.07	0.005	0.007	**ΔE_a× 10^{-16}[erg]**	5174.9 ± 844.7	20.11 ± 0.83	24.37 ± 1.21	63.36 ± 1.80
M_R/M_S	0.271	0.013	0.018					

AC measurements									
	1Hz	**10 Hz**	**100 Hz**	**ΔE_a× 10^{-16}[erg]**	**K_{eff}× 10^5 [erg/cm^3]**	**E_p [erg/cm^2]**	**D_{crit} [nm]**		
							T = 2K	**T = 100K**	**T = 300K**
T_{max1} [K]	295.1	300.1	304.4	1210.3 ± 139.9	0.749 ± 0.134	11.83 ± 1.06 × 10^{-4}	9.73 ± 0.4	11.79 ± 0.59	30.65 ± 3.27
T_{max2} [K]	255.6	269.7	284.7	4066.9 ± 874.8	2.518 ± 0.702	21.68 ± 6.79 × 10^{-4}	17.83 ± 0.74	21.61 ± 1.09	56.18 ± 6.01

3.7. MFT calculations

The thermo-magnetic curve $M(T)$ recorded at 0.1 T and depicted in Figure 10 indicate a visible saturation at the low-temperature range and therefore the influence of domain structure on $M(T)$ is almost inconsiderable. Thus, in this case, one can apply the so-called mean field theory (MFT) calculation in order to estimate the exchange coupling parameters between two magnetic sites denoted as A – A (A_{AA}), B - B (A_{BB}) and A – B (A_{AB}) [122–125]. Herein the applied MFT calculation is a novelty approach to describe magnetic behavior in spinel nanoferrites. The average coordination numbers A – A (Z_{AA}), R–T (Z_{AB}), T–R (Z_{BA}) and B – B (Z_{BB}) surroundings determined based XRD analysis equal 4, 4, 3 and 6 respectively. As it was

shown, the magnetic ordering in Ni – Zn ferrites is caused by super-exchange interactions [1,37,59,79,118]. The magnetic moments of A and B sites with unpaired 3*d* spins are coupled ferromagnetically. Such coupling between magnetic cations is realized via oxygen anions e.g. A – O – B and B – O – B [1,37]. Thus, the exchange interactions are described by the Heisenberg model, where the exchange coupling A_{ij} parameters can be separated for tetrahedral and octahedral sites respectively. According to Néel theory in the case of ferrites with A – B dominant interaction the magnetization (M) is a superposition of the two A (site A) and B (site B) magnetic sublattices, i.e., $M = |M_B - M_A|$. Thus, based on the MFT approximation magnetization in each sites M_A and M_B are described by the following relations [122–125]:

$$\begin{aligned} \boldsymbol{M}_A &= -N_A\mu_B g_A\langle \boldsymbol{J}_A\rangle = -N_A\mu_B g_A \boldsymbol{J}_A B\left(\frac{g_A J_A H_A}{k_B T}\mu_B\right) \\ \boldsymbol{M}_B &= -N_B\mu_B g_B\langle \boldsymbol{J}_B\rangle = -N_B\mu_B g_B \boldsymbol{J}_B B\left(\frac{g_B J_b H_B}{k_B T}\mu_B\right) \end{aligned}, \tag{22}$$

and:

$$\begin{aligned} \boldsymbol{H}_A &= \frac{2A_{AA}Z_{AA}(g_A-1)^2}{N_A g_A^2\mu_B^2}\boldsymbol{M}_A + \frac{2A_{AB}Z_{AB}(g_A-1)(g_B-1)}{N_B g_A g_B\mu_B^2}\boldsymbol{M}_B + H_{EXT} \\ \boldsymbol{H}_B &= \frac{2A_{BA}Z_{BA}(g_B-1)(g_T-1)}{N_A g_A g_B\mu_B^2}\boldsymbol{M}_A + \frac{2A_{BB}Z_{BB}(g_B-1)^2}{N_B g_B^2\mu_B^2}\boldsymbol{M}_B + H_{EXT} \end{aligned}, \tag{23}$$

where $B\left(\frac{g_A J_A H_A}{k_B T}\mu_B\right)$ and $B\left(\frac{g_B J_B H_B}{k_B T}\mu_B\right)$ are the Brillouin functions, N is the number on corresponding atoms per unit volume, μ_B is the Bohr magneton, g is the Landé factor, J is the total angular momentum, H is the magnetic field acting on the corresponding site, H_{EXT} is the external field, k_B is the Boltzmann constant. By using of the equations (22) and (23) one can determine the exchange coupling parameters of A - A (A_{AA}), B - B (A_{BB}) and A - B ($A_{AB} = A_{BA}$) sites via fitting the dependence to the empirical thermo-magnetic curve $M(T)$. With the preliminary assumptions, one can also determine the average magnetic moment per A and B sites.

Thus, the values of exchange coupling parameters obtained from MFT calculations within A (A_{AA}) as well as B (A_{BB}) sites equal 1.01×10^{-21}J and 3.35×10^{-23}J, respectively.

Simultaneously, the value of the exchange coupling parameter between A and B sites (A_{AB}) is negative and equals 8.45×10^{-22} J confirming the antiparallel coupling of both sites. Based on the applied MFT fitting procedure the estimation of the magnetic moment in tetrahedral and octahedral magnetic sublattice and was implemented. Thus, the value of the total magnetization calculated based on MFT and antiparallel A and B sublattices arrangements is estimated as 1.91 μ_B, which is close to the experimental value estimated at the room temperature and strengthens the evidence for the spin canting phenomena. Similarly, the resultant magnetization at the low-temperature range (see Figure 10) is lower than defined from the hysteresis loops.

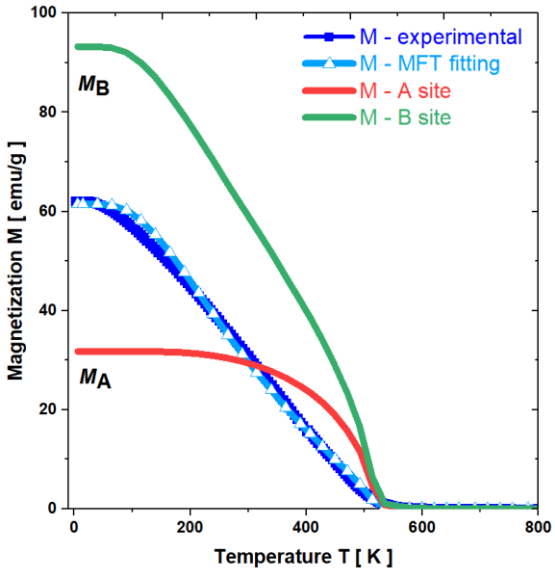

Figure 10. The *M(T)* dependence for $Ni_{0.5}Zn_{0.5}Fe_2O_4$ and its fit by MFT

3.8. Mössbauer spectroscopy

The temperature evolution of the Mössbauer spectra refined consequently by using MOSFIT software, a Lorentzian line-fitting program [126] were illustrated in Figure 11. At high temperature (473K) the spectrum consists of a paramagnetic quadrupolar doublet and as the temperature decreases, magnetic sextet components with a broad line width appears (300K). At low temperatures (77K and 4.2K) the magnetic components become predominant. Indeed, these two components reflect the particles size distribution of the sample. As it was evidenced according to the-F law (19), the relaxation time τ of the magnetic moment fluctuation depends

on volume V of the particle and the temperature T. Thus, the paramagnetic doublet is due to a fast relaxation time τ and corresponds to a low volume size while the magnetic sextet is originated from slow τ and corresponds to a bigger volume. The observed phenomenon was already confirmed by previous investigations [2,38,46,54].

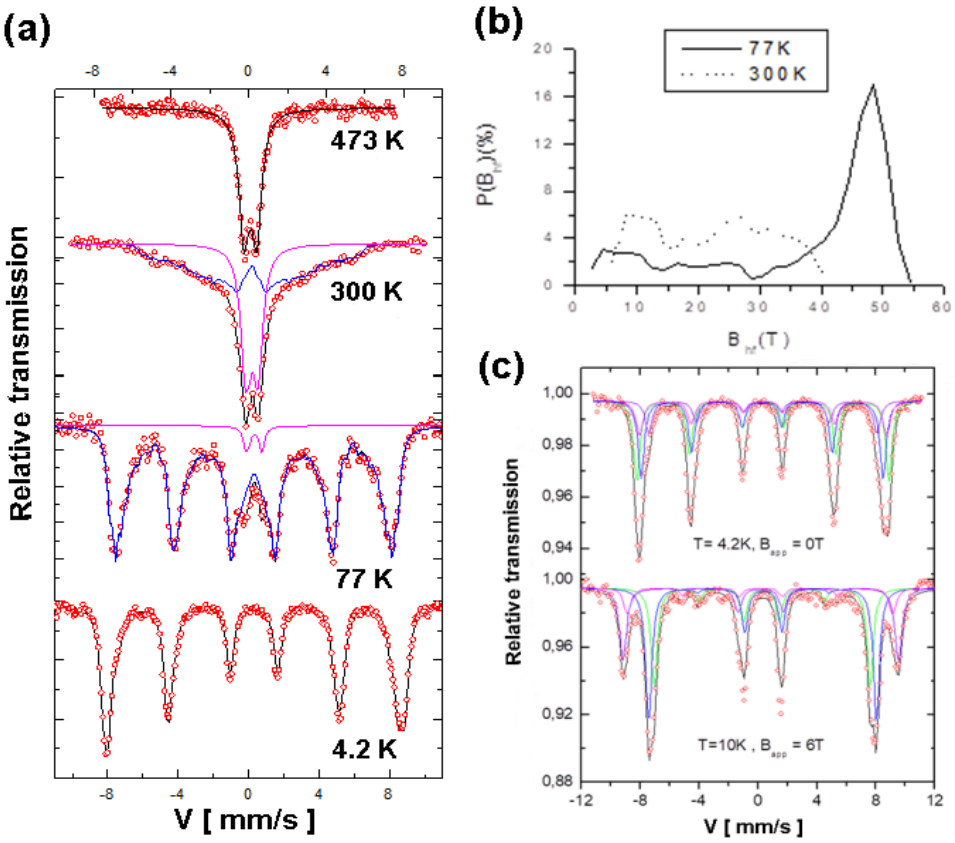

Figure 11. (a) Mössbauer spectra at 473K, 300K, 77K and 4.2K; (b) The percentage distribution of hyperfine field; (c)the comparison between 4.2 K (B_{appl} = 0) and 10 K in-field (B_{appl} = 6 T) spectra for $Ni_{0.5}Zn_{0.5}Fe_2O_4$ spinel nano ferrites.

Taking into account the temperature dependence of spectrum's shape, all spectra were fitted with a model composed of quadrupolar doublet and assembly of magnetic sextets, which consists of a discrete distribution value of hyperfine field (B_{hf}) with fitted but common values of isomer shift (δ), Quadrupolar Splitting/quadrupolar shift (Q.S./2ε). The fitted values of hyperfine parameters are displayed in Table 4. The obtained values of hyperfine parameters (δ and Q.S.) associated with a paramagnetic component characteristic of ferric species Fe^{3+}. As one may notice, when the temperature decreases, magnetic components, revealed by the

presence of large striped sextuplets, emerge at the expense of the decrease of the paramagnetic component. Such evolution of the hyperfine structure is consistent with a slowing of superparamagnetic fluctuations attributed to the decrease in temperature. The common values of isomer shift and values of the quadrupolar splitting of the sextets correspond to that of Fe^{3+} while the mean value of hyperfine field decreases with temperature and relaxation time according to the V-F law.

Figure 11b represents the temperature evolution of the hyperfine field distribution obtained from fitting Mössbauer spectra at 300 K and 77 K temperatures. It provides information about blocking of the magnetic moment of particles by reducing the temperature. The existence of particles size distribution is confirmed by the ZFC-FC as well as AC measurements magnetic measurements. So, at 77K, particles with low volume remain in the superparamagnetic state. At 4.2 K, the spectrum consists only of sextets. So, the superparamagnetic fluctuation completely vanishes and all the magnetic moment are blocked. In this way, the low-temperature spectrum represents an assembly of magnetically ordered states (anti or ferrimagnetic state). This spectrum represents the inverse spinel structure of $Ni_{0.5}Zn_{0.5}Fe_2O_4$ where the Zn^{2+} ions occupied the tetrahedral sites and the Fe^{3+} and Ni^{2+} ions are distributed in tetrahedral and octahedral sites. The mixed spinel ferrite $Ni_{0.5}Zn_{0.5}Fe_2O_4$ has a ferromagnetic behavior with an anti-ferromagnetic exchange coupling between the A - tetrahedral and B - octahedral sites. The mean hyperfine field value of spectrum recorded at 4.2 K tends to 51 T (see the first section in Table 4) and presents a low spectral resolution and then does not allow to distinguish between the two expected components typical for A and B sites respectively. Indeed, in the mixed $Ni_{0.5}Zn_{0.5}Fe_2O_4$inverse spinel Fe^{3+} ions, which occupy both sites have the same value of magnetic moment ($\sim 5\mu_B$) and then the same value of the hyperfine field. In order to resolve the low-temperature spectrum and to estimate the Fe populations located in both sites,in-field Mössbauer measurements were performed. Thus, the Mössbauer

spectra were recorded under external magnetic field with a value of 6 T and 10K. When the external field is applied, one of the sublattice (here A) sees its value of the field increased and the other (B) reduced. In this kind of experiment, the actually observed effective field of tetrahedral B_{eff}^{T} and octahedral B_{eff}^{O} sites denotes the vectorial sum of B_{app} and the internal hyperfine fields B_{hyp} ($B_{eff} = B_{hyp} + B_{app}$) of tetrahedral B_{hyp}^{T} and octahedral B_{hyp}^{O} sites providing useful information about relative orientation between the local magnetic field at the probe nucleus and the external filed (i.e., between B_{app} and the magnetic sublattices). If β is the angle between the effective field and the field applied along the γ radiation, the relationship between the hyperfine field (B_{hyp}), effective field (B_{eff}) and applied field (B_{app}) is given by:

$$B_{hyp}^{2} = B_{eff}^{2} + B_{app}^{2} - 2B_{eff}B_{app}cos\beta \quad (25)$$

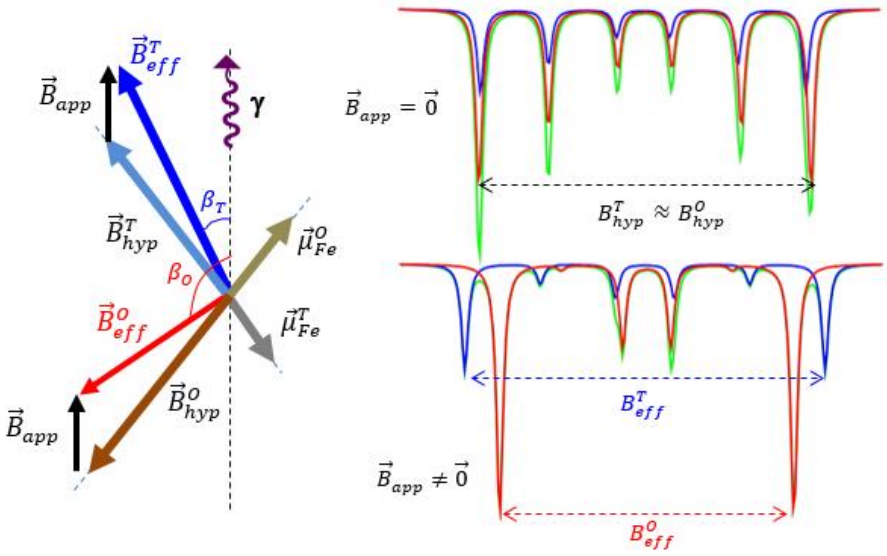

Figure 12. The schematic representation of the vector diagram of the hyperfine field of ions Fe^{3+} in tetrahedral and octahedral sites under an applied magnetic field and corresponding Mössbauer spectra at $B_{appl} = 0$ and $B_{appl} \neq 0$ T for $Ni_{0.5}Zn_{0.5}Fe_2O_4$ spinel nano ferrites.

The comparison between spectrum at 4.2 K and in-field spectrum recorded at 10K is shown in Figure 11c. Taking account the two different sites of Fe^{3+} in the spinel structure with the magnetic moments in tetrahedral site μ_{Fe}^{T} and octahedral site μ_{Fe}^{O} in opposite direction, the refinement of the obtained data required two components, one corresponds to the A sublattice

and the second to the B sublattice. Figure 12 shows the schematic representation of the vector diagram of the hyperfine field of the ions Fe^{3+} in sites A and B under an applied magnetic field. After several fitting runs, the best refinement was obtained by using two components for each sublattice.

The obtained hyperfine parameters values are reported in the second section of Table 4. The difference between the values of isomer shift of B and A sites is in order of $\delta(B)-\delta(A) \approx$ 0.13-15 mm/s, which is similar to the difference expected for γ-Fe_2O_3 iron oxide between both Fe^{3+} sites. The hyperfine field values in order to those of Fe^{3+} oxide minerals in B and A sites. The relative intensities of the lines are linked to the angleβ by the equation:

$$\frac{I_{2,5}}{\sum I_i} = \sin^2 \beta \qquad (26)$$

Table 4: Values of hyperfine parameters for $Ni_{0.5}Zn_{0.5}Fe_2O_4$ spinel nano ferrites

Values of hyperfine parameters as a function of temperature							
T	**Component**	**δ (±0.01) [mm/s]**	**Γ/2 (fixed value) [mm/s]**	**Q.S./2ε (±0.01) [mm/s]**	**B_{hyp} (±2) [T]**	**%**
473K	**paramagnetic**	0.22	0.31	0.61	0	100
300K	**magnetic**	0.32	0.18	0	22	60
	paramagnetic	0.33	0.32	0.62	0	40
77K	**magnetic**	0.43	0.18	0	38	94
	paramagnetic	0.28	0.32	0.51	0	6
4.2K	**magnetic**	0.45	0.16	0	51	100
Hyperfine parameters values recorded at 10K and under the the external field of 6T.							
	δ (±0.01) [mm/s]	**Γ [mm/s]**	**2ε (±0.01) [mm/s]**	**B_{eff} (±2) [T]**	**B_{hf} (±2) [T]**	**β [°] (±2)**	**%**
B1	0.26	0.50	0.01	45	51	25	30
B2	0.33	0.50	-0.06	48	54	12	37
A1	0.16	0.57	-0.05	55	49	38	10
A2	0.18	0.57	-0.04	58	52	11	23

As it presented in Table 4, non-zero values of β angle confirm the canting effect of Fe^{3+} magnetic moments and the non-collinear ferrimagnetic behavior. The percentage ratio Fe^{3+} (A)/ Fe^{3+}(B) ≈ 0.33 represents the ration between Fe^{3+} ions in sites A over those in B sites. The obtained value corresponds to the ideal cationic distribution where half of the A sites and three-quarters of the B sites are occupied by Fe^{3+} ions. The obtained results are in a good agreement with XRD and XPS data.

4. Conclusions

In the present study, the $Ni_{0.5}Zn_{0.5}Fe_2O_4$ nanoferrites were characterized for the first time so widely by various complementary experimental techniques. The purity and phase of the studied sample synthesized by co-precipitation route were confirmed by XRD, FTIR and XPS methods. The performed diffraction studies indicate the cubic inverse spinel ferrite structure with *Fd-3m* space group demonstrating the cations distributions among tetrahedral A – site and octahedral B – site. Raman and FTIR studies confirmed spinel structure with tetrahedrally and octahedrally iron occupancy, indicating the presence of iron-oxide phases. A lattice hydroxyl ‘‘defects’’ localized at octahedral iron vacancies as well as deformation mode of terminal hydroxyl groups (Fe-OH) on the hematite surface or within the octahedrally coordinated iron site in spinel ferrite have been detected. Additionally, low-ordered phases in the form of maghemite, magnetite and other iron-oxide phases have been considered as factors responsible for the structural disorder of nickel-iron spinel structure. The microstructural analysis revealed the presence of ultrafine grained crystallites/particles ranging from 14.78nm ± 2.56 nm (TEM) to 20.38 nm ± 0.02 nm (XRD). The visible discrepancies between particles size estimated by the use of various methods are related to the surface disorder and irregular shapes of nanoparticles, their agglomerations as well as different sensitivity of utilized measurement techniques. Made for the first time the high-resolution XPS spectral analysis of core level lines in the $Ni_{0.5}Zn_{0.5}Fe_2O_4$ nanoferrites after applied ion etching procedure confirmed the

distribution of Fe^{3+} at both A and B sites. Furthermore, it provided an information about the distribution of Ni^{2+} and Zn^{2+} at B and A site respectively. Additionally, the detailed analysis of Fe2*p* core level lines revealed the presence of pure iron clusters.

The detailed investigation of magnetic properties exhibits the ferrimagnetic nature of studied nano ferrites at low temperatures due to the domination of A – B interaction. However, the superparamagnetic behavior confirmed by almost zero coercivity and negligible remanence is found at the room temperature. The canting spin effect on SF – NPs was confirmed based on magnetic properties measurements. The opposite alignment of A and B magnetic sublattices was evidenced experimentally as well as by MFT calculations performed for the first time for such nanoferrites. The values of effective anisotropy constant K_{eff} estimated from DC as well as AC magnetization are in a quite good agreement. The analysis of magnetic parameters as well as Mössbauer spectra may suggest superparamagnetic behavior at the room temperature for studied nanoferrites. Finally, the microstructural and magnetic properties of $Ni_{0.5}Zn_{0.5}Fe_2O_4$ spinel nano ferrites make them attractive candidates due to their possible applications.

References

[1] M.S. Seehra, ed., Magnetic Spinels- Synthesis, Properties and Applications, InTechOpen, 2017.

[2] M. Tsvetkov, M. Milanova, L.C.J. Pereira, J.C. Waerenbourgh, Z. Cherkezova-Zheleva, J. Zaharieva, I. Mitov, Magnetic properties of binary and ternary mixed metal oxides NiFe2O4 and Zn0.5Ni0.5Fe2O4 doped with rare earths by sol—gel synthesis, Chem. Pap. 70 (2016) 1600–1610. doi:10.1515/chempap-2016-0097.

[3] Y.G. Ma, M.Z. Jin, M.L. Liu, G. Chen, Y. Sui, Y. Tian, G.J. Zhang, Y.Q. Jia, Effect of high pressure on Mössbauer spectra of NiFe2O4 ultrafine particles with different grain sizes, Mater. Chem. Phys. 65 (2000) 79–84. doi:10.1016/S0254-0584(00)00212-1.

[4] J. Huo, M. Wei, Characterization and magnetic properties of nanocrystalline nickel ferrite synthesized by hydrothermal method, Mater. Lett. 63 (2009) 1183–1184. doi:10.1016/j.matlet.2009.02.024.

[5] J. Wang, F. Ren, R. Yi, A. Yan, G. Qiu, X. Liu, Solvothermal synthesis and magnetic properties of size-controlled nickel ferrite nanoparticles, J. Alloys Compd. 479 (2009) 791–796. doi:10.1016/j.jallcom.2009.01.059.

[6] K. Maaz, S. Karim, A. Mumtaz, S.K. Hasanain, J. Liu, J.L. Duan, Synthesis and magnetic characterization of nickel ferrite nanoparticles prepared by co-precipitation route, J. Magn. Magn. Mater. 321 (2009) 1838–1842. doi:10.1016/j.jmmm.2008.11.098.

[7] P. Sivakumar, R. Ramesh, A. Ramanand, S. Ponnusamy, C. Muthamizhchelvan, Preparation and properties of nickel ferrite (NiFe2O4) nanoparticles via sol–gel auto-combustion method, Mater. Res. Bull. 46 (2011) 2204–2207. doi:10.1016/j.materresbull.2011.09.010.

[8] C. Luadthong, V. Itthibenchapong, N. Viriya-empikul, K. Faungnawakij, P. Pavasant, W. Tanthapanichakoon, Synthesis, structural characterization, and magnetic property of nanostructured ferrite spinel oxides (AFe2O4, A = Co, Ni and Zn), Mater. Chem. Phys. 143 (2013) 203–208. doi:10.1016/j.matchemphys.2013.08.052.

[9] M.I. Oshtrakh, M.V. Ushakov, B. Senthilkumar, R.K. Selvan, C. Sanjeeviraja, I. Felner, V.A. Semionkin, Study of NiFe2O4 nanoparticles using Mössbauer spectroscopy with a high velocity resolution, Hyperfine Interact. 219 (2013) 7–12. doi:10.1007/s10751-012-0660-1.

[10] M. Kooti, A.N. Sedeh, Synthesis and Characterization of NiFe2O4 Magnetic Nanoparticles by Combustion Method, J. Mater. Sci. Technol. 29 (2013) 34–38. doi:10.1016/j.jmst.2012.11.016.

[11] D. Li, Y. Sun, P. Gao, X. Zhang, H. Ge, Structural and magnetic properties of nickel ferrite nanoparticles synthesized via a template-assisted sol–gel method, Ceram. Int. 40 (2014) 16529–16534. doi:10.1016/j.ceramint.2014.08.006.

[12] T. Shanmugavel, S.G. Raj, G. Rajarajan, G.R. Kumar, Tailoring the Structural and Magnetic Properties and of Nickel Ferrite by Auto Combustion Method, Procedia Mater. Sci. 6 (2014) 1725–1730. doi:10.1016/j.mspro.2014.07.158.

[13] G.D. Park, J.S. Cho, Y.C. Kang, Multiphase and Double-Layer NiFe2O4@NiO-Hollow-Nanosphere-Decorated Reduced Graphene Oxide Composite Powders Prepared by Spray Pyrolysis Applying Nanoscale Kirkendall Diffusion, ACS Appl. Mater. Interfaces. 7 (2015) 16842–16849. doi:10.1021/acsami.5b04891.

[14] T. Shanmugavel, S. Gokul Raj, G. Ramesh Kumar, G. Rajarajan, D. Saravanan, Cost effective preparation and characterization of nanocrystalline nickel ferrites (NiFe2O4) in low temperature regime, J. King Saud Univ. - Sci. 27 (2015) 176–181. doi:10.1016/j.jksus.2014.12.006.

[15] N. Gupta, P. Jain, R. Rana, S. Shrivastava, Current Development in Synthesis and Characterization of Nickel Ferrite Nanoparticle, Mater. Today Proc. 4 (2017) 342–349. doi:10.1016/j.matpr.2017.01.031.

[16] S.M. Hoque, M. Tariq, S.I. Liba, F. Salehin, Z.H. Mahmood, M.N.I. Khan, K. Chattopadhayay, R. Islam, S. Akhter, Thermo-therapeutic applications of chitosan- and PEG-coated NiFe2O4 nanoparticles, Nanotechnology. 27 (2016) 285702. doi:10.1088/0957-4484/27/28/285702.

[17] Z. Ž. Lazarević, Č. Jovalekić, A. Milutinović, D. Sekulić, V.N. Ivanovski, A. Rečnik, B. Cekić, N. Ž. Romčević, Nanodimensional spinel NiFe2O4 and ZnFe2O4 ferrites prepared by soft mechanochemical synthesis, J. Appl. Phys. 113 (2013) 187221. doi:10.1063/1.4801962.

[18] A.S. Fawzi, A.D. Sheikh, V.L. Mathe, Structural, dielectric properties and AC conductivity of Ni(1−x)ZnxFe2O4 spinel ferrites, J. Alloys Compd. 502 (2010) 231–237. doi:10.1016/j.jallcom.2010.04.152.

[19] M. Sertkol, Y. Köseoğlu, A. Baykal, H. Kavas, A. Bozkurt, M.S. Toprak, Microwave synthesis and characterization of Zn-doped nickel ferrite nanoparticles, J. Alloys Compd. 486 (2009) 325–329. doi:10.1016/j.jallcom.2009.06.128.

[20] H. Kavas, A. Baykal, M.S. Toprak, Y. Köseoğlu, M. Sertkol, B. Aktaş, Cation distribution and magnetic properties of Zn doped NiFe2O4 nanoparticles synthesized by PEG-assisted hydrothermal route, J. Alloys Compd. 479 (2009) 49–55. doi:10.1016/j.jallcom.2009.01.014.

[21] A. Verma, T.C. Goel, R.G. Mendiratta, P. Kishan, Magnetic properties of nickel–zinc ferrites prepared by the citrate precursor method, J. Magn. Magn. Mater. 208 (2000) 13–19. doi:10.1016/S0304-8853(99)00585-5.

[22] R.V. Mangalaraja, S. Ananthakumar, P. Manohar, F.D. Gnanam, Magnetic, electrical and dielectric behaviour of Ni0.8Zn0.2Fe2O4 prepared through flash combustion technique, J. Magn. Magn. Mater. 253 (2002) 56–64. doi:10.1016/S0304-8853(02)00413-4.

[23] C. Caizer, M. Stefanescu, Nanocrystallite size effect on σs and Hc in nanoparticle assemblies, Phys. B Condens. Matter. 327 (2003) 129–134. doi:10.1016/S0921-4526(02)01785-4.

[24] H.E. Zhang, B.F. Zhang, G.F. Wang, X.H. Dong, Y. Gao, The structure and magnetic properties of Zn1−xNixFe2O4 ferrite nanoparticles prepared by sol–gel auto-combustion, J. Magn. Magn. Mater. 312 (2007) 126–130. doi:10.1016/j.jmmm.2006.09.016.

[25] M. Sertkol, Y. Köseoğlu, A. Baykal, H. Kavas, A.C. Başaran, Synthesis and magnetic characterization of Zn0.6Ni0.4Fe2O4 nanoparticles via a polyethylene glycol-assisted hydrothermal route, J. Magn. Magn. Mater. 321 (2009) 157–162. doi:10.1016/j.jmmm.2008.08.083.

[26] S. Thakur, S.C. Katyal, M. Singh, Structural and magnetic properties of nano nickel–zinc ferrite synthesized by reverse micelle technique, J. Magn. Magn. Mater. 321 (2009) 1–7. doi:10.1016/j.jmmm.2008.07.009.

[27] M. Sertkol, Y. Köseoğlu, A. Baykal, H. Kavas, M.S. Toprak, Synthesis and magnetic characterization of Zn0.7Ni0.3Fe2O4 nanoparticles via microwave-assisted combustion route, J. Magn. Magn. Mater. 322 (2010) 866–871. doi:10.1016/j.jmmm.2009.11.018.

[28] N.H. Vasoya, L.H. Vanpariya, P.N. Sakariya, M.D. Timbadiya, T.K. Pathak, V.K. Lakhani, K.B. Modi, Synthesis of nanostructured material by mechanical milling and study on structural property modifications in Ni0.5Zn0.5Fe2O4, Ceram. Int. 36 (2010) 947–954. doi:10.1016/j.ceramint.2009.10.024.

[29] T. Jahanbin, M. Hashim, K.A. Matori, S.B. Waje, Influence of sintering temperature on the structural, magnetic and dielectric properties of Ni0.8Zn0.2Fe2O4 synthesized by co-precipitation route, J. Alloys Compd. 503 (2010) 111–117. doi:10.1016/j.jallcom.2010.04.212.

[30] A. Kumar, A. Singh, M.S. Yadav, M. Arora, R.P. Pant, Finite size effect on Ni doped nanocrystalline NixZn1−xFe2O4 (0.1≤x≤0.5), Thin Solid Films. 519 (2010) 1056–1058. doi:10.1016/j.tsf.2010.08.043.

[31] A. Kumar, Annveer, M. Arora, M.S. Yadav, R.P. Panta, Induced size effect on Ni doped Nickel Zinc Ferrite Nanoparticles, Phys. Procedia. 9 (2010) 20–23. doi:10.1016/j.phpro.2010.11.006.

[32] T. Slatineanu, A.R. Iordan, M.N. Palamaru, O.F. Caltun, V. Gafton, L. Leontie, Synthesis and characterization of nanocrystalline Zn ferrites substituted with Ni, Mater. Res. Bull. 46 (2011) 1455–1460. doi:10.1016/j.materresbull.2011.05.002.

[33] S. Kumar, A. Sharma, M. Singh, P. Dhiman, R.K. Kotnala, Size Controlled Synthesis and Magnetic Properties of Ni-Zn Ferrite Nanoparticles by using Aloe Vera Extract Solution : Nano-Journal, (n.d.). http://www.nano-journal.org/detail-nano-journal/58/Size-Controlled-Synthesis-and-Magnetic-Properties-of-Ni-Zn-Ferrite-Nanoparticles-by-using-Aloe-Vera-Extract-Solution-/SANJAY-KUMAR--ASHWANI-SHARMA-M-SINGH-POOJA-DHIMAN-and-R-K-KOTNALA-.html (accessed December 17, 2017).

[34] X. Lu, G. Liang, Q. Sun, C. Yang, High-frequency magnetic properties of Ni-Zn ferrite nanoparticles synthesized by a low temperature chemical method, Mater. Lett. 65 (2011) 674–676. doi:10.1016/j.matlet.2010.11.066.

[35] Č. Jovalekić, A.S. Nikolić, M. Gruden-Pavlović, M.B. Pavlović, Mechanochemical synthesis of stoichiometric nickel and nickel-zinc ferrite powders with Nicolson-Ross analysis of absorption coefficients, J. Serbian Chem. Soc. 77 (2012) 497–505. doi:10.2298/JSC110302186J.

[36] K. Mohit, S.K. Rout, S. Parida, G.P. Singh, S.K. Sharma, S.K. Pradhan, I. Won Kim, Structural, optical and dielectric studies of NixZn1−xFe2O4 prepared by auto combustion route, Phys. B Condens. Matter. 407 (2012) 935–942. doi:10.1016/j.physb.2011.12.003.

[37] E. Ušák, M. Ušáková, Influence of Ni/Zn ratio variation on structural and magnetic properties of NiZn ferrites, J. Electr. Eng. 63 (2012) 141–143.

[38] A.P. Kazin, M.N. Rumyantseva, V.E. Prusakov, I.P. Suzdalev, A.M. Gaskov, Cation distribution in nanocrystalline NixZn1 − xFe2O4 spinel ferrites, Inorg. Mater. 48 (2012) 525–530. doi:10.1134/S002016851205007X.

[39] S.M. Olhero, D. Soma, V.S. Amaral, T.W. Button, F.J. Alves, J.M.F. Ferreira, Co-precipitation of a Ni–Zn ferrite precursor powder: Effects of heat treatment conditions and deagglomeration on the structure and magnetic properties, J. Eur. Ceram. Soc. 32 (2012) 2469–2476. doi:10.1016/j.jeurceramsoc.2012.03.017.

[40] T.J. Shinde, A.B. Gadkari, P.N. Vasambekar, Magnetic properties and cation distribution study of nanocrystalline Ni–Zn ferrites, J. Magn. Magn. Mater. 333 (2013) 152–155. doi:10.1016/j.jmmm.2012.12.049.

[41] R. Sharma, S. Singhal, Structural, magnetic and electrical properties of zinc doped nickel ferrite and their application in photo catalytic degradation of methylene blue, Phys. B Condens. Matter. 414 (2013) 83–90. doi:10.1016/j.physb.2013.01.015.

[42] S.J. Azhagushanmugam, N. Suriyanarayanan, R. Jayaprakash, Synthesis and Characterization of Nanocrystalline Ni(0.6) Zn(0.4) Fe2O4 Spinel Ferrite Magnetic Material, Phys. Procedia. 49 (2013) 44–48. doi:10.1016/j.phpro.2013.10.009.

[43] M.A. Gabal, S. Kosa, T.S. Al Mutairi, Structural and magnetic properties of Ni1−xZnxFe2O4 nano-crystalline ferrites prepared via novel chitosan method, J. Mol. Struct. 1063 (2014) 269–273. doi:10.1016/j.molstruc.2014.01.070.

[44] R.R. Rathi, P. Joshi, R. Neogi, Auto combustion synthesis of Mg doped Ni-Zn ferrite nanoparticle and their characterization, Int. J. Chem. Phys. Sci. 5 (2015) 1–8.

[45] R. Kumar, H. Kumar, R.R. Singh, P.B. Barman, Structural analysis of emerging ferrite: Doped nickel zinc ferrite, AIP Conf. Proc. 1675 (2015) 030003. doi:10.1063/1.4929219.

[46] C. Srinivas, B.V. Tirupanyam, S.S. Meena, S.M. Yusuf, C.S. Babu, K.S. Ramakrishna, D.M. Potukuchi, D.L. Sastry, Structural and magnetic characterization of co-precipitated NixZn1−xFe2O4 ferrite nanoparticles, J. Magn. Magn. Mater. 407 (2016) 135–141. doi:10.1016/j.jmmm.2016.01.060.

[47] G. Uzma, Effect of Si on the dielectric properties of NixZn1 – xFe2O4 as a function of composition and frequency, Indian J. Pure Appl. Phys. 53 (n.d.) 271–273.

[48] S. Kasam, T. Bhargavi, Structural and AC conductivity studies of Ni-Zn ferrite prepared through coprecipitation method, Int. J. Basic Appl. Sci. 1 (n.d.) 4–8.

[49] M. Kurian, D.S. Nair, Effect of preparation conditions on Nickel Zinc Ferrite nanoparticles: A comparison between sol–gel auto combustion and co-precipitation methods, J. Saudi Chem. Soc. 20 (2016) S517–S522. doi:10.1016/j.jscs.2013.03.003.

[50] S.S. Deshmukh, A.V. Humbe, A. Kumar, R.G. Dorik, K.M. Jadhav, Urea assisted synthesis of Ni1−xZnxFe2O4 ($0 \leq x \leq 0.8$): Magnetic and Mössbauer investigations, J. Alloys Compd. Complete (2017) 227–236. doi:10.1016/j.jallcom.2017.01.176.

[51] N. Chandamma, B.M. Manohara, B.S. Ujjinappa, G.J. Shankarmurthy, M.V. Santhosh Kumar, Structural and electrical properties of Zinc doped Nickel ferrites nanoparticles prepared via facile combustion technique, J. Alloys Compd. 702 (2017) 479–488. doi:10.1016/j.jallcom.2016.12.392.

[52] M.K. Anupama, B. Rudraswamy, N. Dhananjaya, Investigation on impedance response and dielectric relaxation of Ni-Zn ferrites prepared by self-combustion technique, J. Alloys Compd. 706 (2017) 554–561. doi:10.1016/j.jallcom.2017.02.241.

[53] A. Hajalilou, H.M. Kamari, K. Shameli, Dielectric and electrical characteristics of mechanically synthesized Ni-Zn ferrite nanoparticles, J. Alloys Compd. 708 (2017) 813–826. doi:10.1016/j.jallcom.2017.03.030.

[54] R. Mondal, S. Dey, S. Majumder, A. Poddar, P. Dasgupta, S. Kumar, Study on magnetic and hyperfine properties of mechanically milled Ni0.4Zn0.6Fe2O4 nanoparticles, J. Magn. Magn. Mater. 448 (2018) 135–145. doi:10.1016/j.jmmm.2017.07.031.

[55] M.A. Ahmed, E. Ateia, L.M. Salah, A.A. El-Gamal, Structural and electrical studies on La3+ substituted Ni–Zn ferrites, Mater. Chem. Phys. 92 (2005) 310–321. doi:10.1016/j.matchemphys.2004.05.049.

[56] S.E. Shirsath, B.G. Toksha, R.H. Kadam, S.M. Patange, D.R. Mane, G.S. Jangam, A. Ghasemi, Doping effect of Mn2+ on the magnetic behavior in Ni–Zn ferrite nanoparticles prepared by sol–gel auto-combustion, J. Phys. Chem. Solids. 71 (2010) 1669–1675. doi:10.1016/j.jpcs.2010.08.016.

[57] V.V. Awati, S.M. Rathod, S.E. Shirsath, M.L. Mane, Fabrication of Cu2+ substituted nanocrystalline Ni–Zn ferrite by solution combustion route: Investigations on structure, cation occupancy and magnetic behavior, J. Alloys Compd. 553 (2013) 157–162. doi:10.1016/j.jallcom.2012.11.045.

[58] Z.Ž. Lazarević, A.N. Milutinović, Č.D. Jovalekić, V.N. Ivanovski, N. Daneu, I. Mađarević, N.Ž. Romčević, Spectroscopy investigation of nanostructured nickel–zinc

ferrite obtained by mechanochemical synthesis, Mater. Res. Bull. 63 (2015) 239–247. doi:10.1016/j.materresbull.2014.12.005.

[59] N.S.S. Murthy, M.G. Natera, S.I. Youssef, R.J. Begum, C.M. Srivastava, Yafet-Kittel Angles in Zinc-Nickel Ferrites, Phys. Rev. 181 (1969) 969–977. doi:10.1103/PhysRev.181.969.

[60] S. Yáñez-Vilar, M. Sánchez-Andújar, C. Gómez-Aguirre, J. Mira, M.A. Señarís-Rodríguez, S. Castro-García, A simple solvothermal synthesis of MFe2O4 (M=Mn, Co and Ni) nanoparticles, J. Solid State Chem. 182 (2009) 2685–2690. doi:10.1016/j.jssc.2009.07.028.

[61] J. Bennet, R. Tholkappiyan, K. Vishista, N.V. Jaya, F. Hamed, Attestation in self-propagating combustion approach of spinel AFe2O4 (A=Co, Mg and Mn) complexes bearing mixed oxidation states: Magnetostructural properties, Appl. Surf. Sci. 383 (2016) 113–125. doi:10.1016/j.apsusc.2016.04.177.

[62] H. El Moussaoui, T. Mahfoud, S. Habouti, K. El Maalam, M. Ben Ali, M. Hamedoun, O. Mounkachi, R. Masrour, E.K. Hlil, A. Benyoussef, Synthesis and magnetic properties of tin spinel ferrites doped manganese, J. Magn. Magn. Mater. 405 (2016) 181–186. doi:10.1016/j.jmmm.2015.12.059.

[63] F. Bensebaa, F. Zavaliche, P. L'Ecuyer, R.W. Cochrane, T. Veres, Microwave synthesis and characterization of Co–ferrite nanoparticles, J. Colloid Interface Sci. 277 (2004) 104–110. doi:10.1016/j.jcis.2004.04.016.

[64] P.P.C. Sartoratto, M.A.G. Soler, T.M. Lima, F.L.R. Silva, T.V. Trufini, V.K. Garg, A.C. Oliveira, P.C. Morais, Size-modulation of thermally-annealed nanosized cobalt ferrite particles, Phys. Procedia. 9 (2010) 10–14. doi:10.1016/j.phpro.2010.11.004.

[65] D. Peddis, M.V. Mansilla, S. Mørup, C. Cannas, A. Musinu, G. Piccaluga, F. D'Orazio, F. Lucari, D. Fiorani, Spin-Canting and Magnetic Anisotropy in Ultrasmall CoFe2O4 Nanoparticles, J. Phys. Chem. B. 112 (2008) 8507–8513. doi:10.1021/jp8016634.

[66] B. Babić-Stojić, V. Jokanović, D. Milivojević, Z. Jagličić, D. Makovec, N. Jović, M. Marinović-Cincović, Magnetic and Structural Studies of CoFe2O4 Nanoparticles Suspended in an Organic Liquid, J. Nanomater. (2013). doi:10.1155/2013/741036.

[67] N.V. Long, Y. Yang, T. Teranishi, C.M. Thi, Y. Cao, M. Nogami, Related magnetic properties of CoFe2O4 cobalt ferrite particles synthesised by the polyol method with NaBH4 and heat treatment: new micro and nanoscale structures, RSC Adv. 5 (2015) 56560–56569. doi:10.1039/C5RA10015A.

[68] I.S. Lyubutin, N.E. Gervits, S.S. Starchikov, C.-R. Lin, Y.-T. Tseng, K.-Y. Shih, Cheng-Chien Wang, I.-H. Chen, Y.L. Ogarkova, N.Y. Korotkov, Magnetic and Mössbauer spectroscopy studies of hollow microcapsules made of silica-coated CoFe 2 O 4 nanoparticles, Smart Mater. Struct. 25 (2016) 015022. doi:10.1088/0964-1726/25/1/015022.

[69] I. Sharifi, H. Shokrollahi, Nanostructural, magnetic and Mössbauer studies of nanosized Co1−xZnxFe2O4 synthesized by co-precipitation, J. Magn. Magn. Mater. 324 (2012) 2397–2403. doi:10.1016/j.jmmm.2012.03.008.

[70] J. Manna, S. Akbayrak, S. Özkar, Nickel(0) nanoparticles supported on bare or coated cobalt ferrite as highly active, magnetically isolable and reusable catalyst for hydrolytic dehydrogenation of ammonia borane, J. Colloid Interface Sci. 508 (2017) 359–368. doi:10.1016/j.jcis.2017.08.045.

[71] Z. Gu, X. Xiang, G. Fan, F. Li, Facile Synthesis and Characterization of Cobalt Ferrite Nanocrystals via a Simple Reduction−Oxidation Route, J. Phys. Chem. C. 112 (2008) 18459–18466. doi:10.1021/jp806682q.

[72] T.M. de L. Alves, B.F. Amorim, M.A.M. Torres, C.G. Bezerra, S.N. de Medeiros, P.L. Gastelois, L.E.F. Outon, W.A. de A. Macedo, Wasp-waisted behavior in magnetic hysteresis curves of CoFe2O4 nanopowder at a low temperature: experimental evidence and theoretical approach, RSC Adv. 7 (2017) 22187–22196. doi:10.1039/C6RA28727A.

[73] I. Sharifi, H. Shokrollahi, M.M. Doroodmand, R. Safi, Magnetic and structural studies on CoFe2O4 nanoparticles synthesized by co-precipitation, normal micelles and reverse micelles methods, J. Magn. Magn. Mater. 324 (2012) 1854–1861. doi:10.1016/j.jmmm.2012.01.015.

[74] S. Bhukal, T. Namgyal, S. Mor, S. Bansal, S. Singhal, Structural, electrical, optical and magnetic properties of chromium substituted Co–Zn nanoferrites Co0.6Zn0.4CrxFe2−xO4 (0≤x≤1.0) prepared via sol–gel auto-combustion method, J. Mol. Struct. 1012 (2012) 162–167. doi:10.1016/j.molstruc.2011.12.019.

[75] L. Pérez-Mirabet, E. Solano, F. Martínez-Julián, R. Guzmán, J. Arbiol, T. Puig, X. Obradors, A. Pomar, R. Yáñez, J. Ros, S. Ricart, One-pot synthesis of stable colloidal solutions of MFe2O4 nanoparticles using oleylamine as solvent and stabilizer, Mater. Res. Bull. 48 (2013) 966–972. doi:10.1016/j.materresbull.2012.11.086.

[76] I. Sharifi, H. Shokrollahi, Structural, Magnetic and Mössbauer evaluation of Mn substituted Co–Zn ferrite nanoparticles synthesized by co-precipitation, J. Magn. Magn. Mater. 334 (2013) 36–40. doi:10.1016/j.jmmm.2013.01.021.

[77] M.A. Amer, T.M. Meaz, A.G. Mostafa, M. El-Kastawi, A.I. Ghoneim, Characterization and spectral studies of Co3+-doped Cd0.4Mn0.6Fe2O4 ferrites, Ceram. Int. 40 (2014) 241–248. doi:10.1016/j.ceramint.2013.05.130.

[78] A.A. Ati, Z. Othaman, A. Samavati, Influence of cobalt on structural and magnetic properties of nickel ferrite nanoparticles, J. Mol. Struct. 1052 (2013) 177–182. doi:10.1016/j.molstruc.2013.08.040.

[79] R. Topkaya, A. Baykal, A. Demir, Yafet–Kittel-type magnetic order in Zn-substituted cobalt ferrite nanoparticles with uniaxial anisotropy, J. Nanoparticle Res. 15 (2013) 1359. doi:10.1007/s11051-012-1359-6.

[80] N. Guskos, S. Glenis, J. Typek, G. Zolnierkiewicz, P. Berczynski, K. Wardal, A. Guskos, D. Sibera, D. Moszyński, W. Lojkowski, U. Narkiewicz, Magnetic properties of ZnFe2O4 nanoparticles, Open Phys. 10 (2012) 470–477. doi:10.2478/s11534-012-0013-3.

[81] M.H. Sousa, F.A. Tourinho, J.C. Rubim, Use of Raman micro-spectroscopy in the characterization of MIIFe2O4 (M = Fe, Zn) electric double layer ferrofluids, J. Raman Spectrosc. 31 (2000) 185–191. doi:10.1002/(SICI)1097-4555(200003)31:3<185::AID-JRS511>3.0.CO;2-B.

[82] J. Liu, M. Zeng, R. Yu, Surfactant-free synthesis of octahedral ZnO/$ZnFe_2O_4$ heterostructure with ultrahigh and selective adsorption capacity of malachite green, Sci. Rep. 6 (2016) 25074. doi:10.1038/srep25074.

[83] S. Bera, A. a. M. Prince, S. Velmurugan, P.S. Raghavan, R. Gopalan, G. Panneerselvam, S.V. Narasimhan, Formation of zinc ferrite by solid-state reaction and its characterization by XRD and XPS, J. Mater. Sci. 36 (2001) 5379–5384. doi:10.1023/A:1012488422484.

[84] V. Šepelák, S. Bégin-Colin, G.L. Caër, Transformations in oxides induced by high-energy ball-milling, Dalton Trans. 41 (2012) 11927–11948. doi:10.1039/C2DT30349C.

[85] V. Šepelák, K.D. Becker, Comparison of the cation inversion parameter of the nanoscale milled spinel ferrites with that of the quenched bulk materials, Mater. Sci. Eng. A. 375–377 (2004) 861–864. doi:10.1016/j.msea.2003.10.178.

[86] S. Thota, S.C. Kashyap, S.K. Sharma, V.R. Reddy, Cation distribution in Ni-substituted Mn0.5Zn0.5Fe2O4 nanoparticles: A Raman, Mössbauer, X-ray diffraction and electron spectroscopy study, Mater. Sci. Eng. B. 206 (2016) 69–78. doi:10.1016/j.mseb.2016.01.002.

[87] R. Tholkappiyan, K. Vishista, Combustion synthesis of Mg–Er ferrite nanoparticles: Cation distribution and structural, optical, and magnetic properties, Mater. Sci. Semicond. Process. 40 (2015) 631–642. doi:10.1016/j.mssp.2015.06.076.

[88] M. Srivastava, S. Chaubey, A.K. Ojha, Investigation on size dependent structural and magnetic behavior of nickel ferrite nanoparticles prepared by sol–gel and hydrothermal methods, Mater. Chem. Phys. 118 (2009) 174–180. doi:10.1016/j.matchemphys.2009.07.023.

[89] S. Kumar, A. Sharma, M. Singh, P. Dhiman, R.K. Kotnala, Size Controlled Synthesis and Magnetic Properties of Ni-Zn Ferrite Nanoparticles by using Aloe Vera Extract Solution, Nano Vis. 1 (2011) 101–114.

[90] M.A. Gabal, Y.M. Al Angari, M.W. Kadi, Structural and magnetic properties of nanocrystalline Ni1−xCuxFe2O4 prepared through oxalates precursors, Polyhedron. 30 (2011) 1185–1190. doi:10.1016/j.poly.2011.01.032.

[91] G. Mie, Beiträge zur Optik trüber Medien, speziell kolloidaler Metallösungen, Ann. Phys. 330 (1908) 377–445. doi:10.1002/andp.19083300302.

[92] H. Horvath, Gustav Mie and the scattering and absorption of light by particles: Historic developments and basics, J. Quant. Spectrosc. Radiat. Transf. 110 (2009) 787–799. doi:10.1016/j.jqsrt.2009.02.022.

[93] S.A. Mazen, M.H. Abdallah, B.A. Sabrah, H. a. M. Hashem, The Effect of Titanium on Some Physical Properties of CuFe2O4, Phys. Status Solidi A. 134 (1992) 263–271. doi:10.1002/pssa.2211340123.

[94] J. Kreisel, G. Lucazeau, H. Vincent, Raman Spectra and Vibrational Analysis of BaFe12O19Hexagonal Ferrite, J. Solid State Chem. 137 (1998) 127–137. doi:10.1006/jssc.1997.7737.

[95] I.V. Chernyshova, M.F.H. Jr, A.S. Madden, Size-dependent structural transformations of hematite nanoparticles. 1. Phase transition, Phys. Chem. Chem. Phys. 9 (2007) 1736–1750. doi:10.1039/B618790K.

[96] A. Ebrahiminezhad, Y. Ghasemi, S. Rasoul-Amini, J. Barar, S. Davaran, Impact of Amino-Acid Coating on the Synthesis and Characteristics of Iron-Oxide Nanoparticles (IONs), Bull. Korean Chem. Soc. 33 (2012) 3957–3962. doi:10.5012/bkcs.2012.33.12.3957.

[97] J.L. Jambor, J.E. Dutrizac, Occurrence and Constitution of Natural and Synthetic Ferrihydrite, a Widespread Iron Oxyhydroxide, Chem. Rev. 98 (1998) 2549–2586. doi:10.1021/cr970105t.

[98] A.A. Khaleel, Nanostructured Pure γ-Fe2O3 via Forced Precipitation in an Organic Solvent, Chem. – Eur. J. 10 (2004) 925–932. doi:10.1002/chem.200305135.

[99] H. Fan, B. Song, Z. Yang, Q. Li, Induced nucleation of haematite nanoparticles with superparamagnetic properties, Nanotechnology. 16 (2005) 1100. doi:10.1088/0957-4484/16/8/018.

[100] G.W. Brady, C.R. Kurkjian, E.F.X. Lyden, M.B. Robin, P. Saltman, T. Spiro, A. Terzis, The structure of an iron core analog of ferritin, Biochemistry (Mosc.). 7 (1968) 2185–2192. doi:10.1021/bi00846a022.

[101] S.J. Oh, D.C. Cook, H.E. Townsend, Characterization of Iron Oxides Commonly Formed as Corrosion Products on Steel, Hyperfine Interact. 112 (1998) 59–66. doi:10.1023/A:1011076308501.

[102] U. Schwertmann, W.R. Fischer, Natural "amorphous" ferric hydroxide, Geoderma. 10 (1973) 237–247. doi:10.1016/0016-7061(73)90066-9.

[103] A. Voegelin, S.J. Hug, Catalyzed Oxidation of Arsenic(III) by Hydrogen Peroxide on the Surface of Ferrihydrite: An in Situ ATR-FTIR Study, Environ. Sci. Technol. 37 (2003) 972–978. doi:10.1021/es025845k.

[104] L. Mazzetti, P.J. Thistlethwaite, Raman spectra and thermal transformations of ferrihydrite and schwertmannite, J. Raman Spectrosc. 33 (2002) 104–111. doi:10.1002/jrs.830.

[105] E. Murad, J.L. Bishop, The infrared spectrum of synthetic akaganéite, β-FeOOH, Am. Mineral. 85 (2015) 716–721. doi:10.2138/am-2000-5-609.

[106] J.T. Keiser, C.W. Brown, R.H. Heidersbach, Characterization of the passive film formed on weathering steels, Corros. Sci. 23 (1983) 251–259. doi:10.1016/0010-938X(83)90106-3.

[107] V. Barrón, J. Torrent, E. de Grave, Hydromaghemite, an intermediate in the hydrothermal transformation of 2-line ferrihydrite into hematite, Am. Mineral. 88 (2003) 1679–1688. doi:10.2138/am-2003-11-1207.

[108] P.S.R. Prasad, K. Shiva Prasad, V. Krishna Chaitanya, E.V.S.S.K. Babu, B. Sreedhar, S. Ramana Murthy, In situ FTIR study on the dehydration of natural goethite, J. Asian Earth Sci. 27 (2006) 503–511. doi:10.1016/j.jseaes.2005.05.005.

[109] M.P. Morales, N.O. Nuñez, R. Pozas, M. Ocaña, C.J. Serna, Determination of the Orientation of the Crystallographic Axes in Anisometric Particles by Infrared Spectroscopy, Appl. Spectrosc. 56 (2002) 200–204.

[110] Y. Shi, J. Ding, Z.X. Shen, W.X. Sun, L. Wang, Strong uni-directional anisotropy in disordered NiFe2O4, Solid State Commun. 115 (2000) 237–241. doi:10.1016/S0038-1098(00)00176-9.

[111] P.R. Graves, C. Johnston, J.J. Campaniello, Raman scattering in spinel structure ferrites, Mater. Res. Bull. 23 (1988) 1651–1660. doi:10.1016/0025-5408(88)90255-3.

[112] K.B. Modi, P.Y. Raval, S.J. Shah, C.R. Kathad, S.V. Dulera, M.V. Popat, K.B. Zankat, K.G. Saija, T.K. Pathak, N.H. Vasoya, V.K. Lakhani, U. Chandra, P.K. Jha, Raman and Mossbauer Spectroscopy and X-ray Diffractometry Studies on Quenched Copper–Ferri–Aluminates, Inorg. Chem. 54 (2015) 1543–1555. doi:10.1021/ic502497a.

[113] Z. Cvejic, S. Rakic, A. Kremenovic, B. Antic, C. Jovalekic, P. Colomban, Nanosize ferrites obtained by ball milling: Crystal structure, cation distribution, size-strain analysis

and Raman investigations, Solid State Sci. 8 (2006) 908–915. doi:10.1016/j.solidstatesciences.2006.02.041.

[114] J.P. Singh, R.C. Srivastava, H.M. Agrawal, R. Kumar, Micro-Raman investigation of nanosized zinc ferrite: effect of crystallite size and fluence of irradiation, J. Raman Spectrosc. 42 (2011) 1510–1517. doi:10.1002/jrs.2902.

[115] I. Morke, A. Stasch, P. Wachter, I. Morke, A. Stasch, P Wachter (1980). Magnons in Raman scattering of magnetite, Hevetica Phys. Acta. 53 (1980) 582–582.

[116] S.V. Jadhav, D.S. Nikam, V.M. Khot, N.D. Thorat, M.R. Phadatare, R.S. Ningthoujam, A.B. Salunkhe, S.H. Pawar, Studies on colloidal stability of PVP-coated LSMO nanoparticles for magnetic fluid hyperthermia, New J. Chem. 37 (2013) 3121–3130. doi:10.1039/C3NJ00554B.

[117] D. Nečas, P. Klapetek, Gwyddion: an open-source software for SPM data analysis, Cent. Eur. J. Phys. 10 (2012) 181–188. doi:10.2478/s11534-011-0096-2.

[118] Y. Yafet, C. Kittel, Antiferromagnetic Arrangements in Ferrites, Phys. Rev. 87 (1952) 290–294. doi:10.1103/PhysRev.87.290.

[119] E.C. Stoner, E.P. Wohlfarth, A mechanism of magnetic hysteresis in heterogeneous alloys, IEEE Trans. Magn. 27 (1991) 3475–3518. doi:10.1109/TMAG.1991.1183750.

[120] J.L. Dormann, D. Fiorani, E. Tronc, Magnetic Relaxation in Fine-Particle Systems, in: I. Prigogine, S.A. Rice (Eds.), Adv. Chem. Phys., John Wiley & Sons, Inc., 1997: pp. 283–494. doi:10.1002/9780470141571.ch4.

[121] G.F. Goya, F.C. Fonseca, R.F. Jardim, R. Muccillo, N.L.V. Carreño, E. Longo, E.R. Leite, Magnetic dynamics of single-domain Ni nanoparticles, J. Appl. Phys. 93 (2003) 6531–6533. doi:10.1063/1.1540032.

[122] A. Hassini, H. Lassri, A. Bouhdada, M. Ayadi, R. Krishnan, I. Mansouri, B. Chaker, Magnetic coupling in amorphous Fe80−xGdxB20 alloys, Phys. B Condens. Matter. 275 (2000) 295–300. doi:10.1016/S0921-4526(99)00752-8.

[123] K. Yano, Molecular field analysis for melt-spun amorphous Fe100−xGdx alloys (18≤X≤60), J. Magn. Magn. Mater. 208 (2000) 207–216. doi:10.1016/S0304-8853(99)00517-X.

[124] A. Bajorek, A. Chrobak, K. Ociepka, G. Chełkowska, The analysis of the magnetic properties and the electronic structure in the TbxGd1−xFe3 intermetallics, Intermetallics. 43 (2013) 110–120. doi:10.1016/j.intermet.2013.07.020.

[125] A. Bajorek, A. Chrobak, G. Chełkowska, K. Ociepka, Magnetism in the YxGd1−xFe3 system, J. Magn. Magn. Mater. 395 (2015) 221–228. doi:10.1016/j.jmmm.2015.07.084.

[126] J. Teillet, F. Varret, unpublished MOSFIT program, Unpubl. MOSFIT Program. (n.d.).

[127] L. Lutterotti, H. Wenk, S. Matthies, MAUD (Material Analysis Using Diffraction): a user friendly Java program for Rietveld Texture Analysis and more, in: NRC Research Press, 1999: pp. 1599–1604. https://iris.unitn.it/handle/11572/57067#.Wjooct_iZaQ (accessed December 20, 2017).

[128] A. Ahlawat, V.G. Sathe, Raman study of NiFe2O4 nanoparticles, bulk and films: effect of laser power, J. Raman Spectrosc. 42 (2011) 1087–1094. doi:10.1002/jrs.2791.